Acta Pharmaceutica Sinica B 2025;15(6):3273−3290

Chinese Pharmaceutical Association
Institute of Materia Medica, Chinese Academy of Medical Sciences

Acta Pharmaceutica Sinica B

www.elsevier.com/locate/apsb
www.sciencedirect.com

ORIGINAL ARTICLE

A chemotherapy nano-booster unlocks wider therapeutic window for prostate cancer treatment

Rui Liao[a,†], Yuequan Wang[a,†], Ziqi Lin[a], Yuting Wang[a], Hongyuan Zhang[a], Qin Chen[c], Shenwu Zhang[a,b], Jin Sun[a,b], Zhonggui He[a,b], Cong Luo[a,b,*]

[a]*Department of Pharmaceutics, Wuya College of Innovation, Shenyang Pharmaceutical University, Shenyang, 110016, China*
[b]*Joint International Research Laboratory of Intelligent Drug Delivery Systems, Ministry of Education, Shenyang Pharmaceutical University, Shenyang, 110016, China*
[c]*Department of Pharmacy, Cancer Hospital of China Medical University, Liaoning Cancer Hospital & Institute, Shenyang, 110042, China*

Received 29 September 2024; received in revised form 30 December 2024; accepted 12 January 2025

KEY WORDS

Prostate cancer treatment;
Gossypol;
Cabazitaxel;
Chemotherapeutic enhancer;
Precise dual-drug nanoassembly;
Therapeutic window broadening;
Carrier-free nanoassembly;
Cancer chemotherapy

Abstract Clinical chemotherapy for prostate cancer is still compromised by high treatment thresholds and severe off-target toxicity of drugs. Given the limited progress in improving therapeutic outcomes and reducing toxicity with the existing toolbox, efforts to broaden the chemotherapeutic window are highly desired. Here, we discover that gossypol (GSP, a natural compound) dramatically enhances the chemosensitivity of cabazitaxel (CTX), even at previously ineffective concentrations. Based on this interesting finding, we exploit a carrier-free chemotherapeutic nano-booster for prostate cancer treatment, which is molecularly co-assembled by GSP and cabazitaxel (CTX). GSP not only readily forms nanoassembly with CTX, but also functions as a chemotherapeutic enhancer that unlocks an ultra-low-dose chemotherapeutic window. Not only that, precise dual-drug nanoassembly confers CTX a significantly larger maximum tolerable dose. As expected, the nano-booster exerts striking therapeutic benefits in mouse prostate tumor xenograft models. This study advances chemotherapeutic window expansion and self-sensitized chemotherapy toward clinical applicability.

*Corresponding author.
E-mail address: luocong@syphu.edu.cn (Cong Luo).
†These authors made equal contributions to this work.
Peer review under the responsibility of Chinese Pharmaceutical Association and Institute of Materia Medica, Chinese Academy of Medical Sciences.

https://doi.org/10.1016/j.apsb.2025.03.029

1. Introduction

Prostate cancer is a serious threat to men's health with high morbidity and mortality[1,2]. However, clinical treatment of prostate cancer remains challenging. Despite the rapid progress of targeted therapy and immunotherapy, the clinical application of these new anticancer modalities still falls short of expectations[3-5]. Owing to the genome instability and mutability of prostate cancer cells, single target-based anticancer therapeutics inevitably suffer from drug resistance, including targeted drugs and immune checkpoint inhibitors[6-10]. Currently, surgery, chemotherapy, endocrinotherapy, and radiotherapy remain staples of cancer treatments applied in clinics. Among them, chemotherapy plays a vital role in treating inoperable patients[1,2.] Notably, most conventional chemotherapeutics, unlike targeted drugs, do not act on specific single targets in cancer cells. Rather, chemotherapeutic drugs gain a therapeutic advantage by exploiting the speed difference of cell proliferation between normal and tumor cells, offering a broad-spectrum approach and often serving as a last resort against multi-resistant cancers that have received targeted therapy or immunotherapy[11-14]. Clinical studies have shown that prostate cancer cells are particularly sensitive to mitotic spindle inhibitors. Cabazitaxel (CTX), a second-generation semi-synthetic taxane, is highly effective against prostate cancer cells by promoting microtubule polymerization, inhibiting depolymerization, and preventing spindle formation. CTX has been approved to treat prostate cancer. However, the clinical potential of CTX is grossly underestimated due to its unsatisfactory therapeutic efficacy and severe off-target toxicity.

Biomedical nanotechnology has played a significant role in advancing anticancer drug delivery[15-17]. Over the past half-century, chemotherapeutic nanomedicines have made remarkable progress in clinical cancer treatment, especially liposomal and micellar nano-formulations[6,18-20]. Several nanomedicines have been approved for clinical use, such as nanoparticle albumin-bound-paclitaxel (Abraxane®) and liposomal doxorubicin (Doxil®)[21-23]. Despite significant progress, currently available nanomedicines still fall short of expectations. Particularly, chemotherapeutic nanomedicines have faced long-standing criticism for their unsatisfactory therapeutic efficacy, even with negligible advantages over conventional formulations[24]. It is worth noting that nanomedicines substantially enhance the safety of antineoplastic agents, a well-recognized strength of biomedical nanotechnology in the context of anticancer drug delivery[25]. However, the use of nanocarriers has not effectively alleviated the issue of off-target toxicity associated with chemotherapeutics. For instance, although Doxil® notably decreases the cardiac toxicity risks of doxorubicin, it is associated with a high incidence of hand and foot syndrome observed in cancer patients receiving multiple intravenous doses of Doxil®[26,27]. Obviously, biomedical nanotechnology has not delivered the expected benefits in tumor-specific drug delivery. Significantly, growing evidence indicates that the inferior clinical outcomes of conventional chemotherapeutic nanomedicines could be attributed to the very limited improvement of tumor-specific drug accumulation with nanocarriers, even less than 0.7% of the total doses in most reported clinical cases[28,29].

Over the past decades, a subset of active-targeting nanomedicines has been fabricated by decorating specific ligands on nanocarriers, both chemical and biological, with the expectation of enhancing drug accumulation through specific recognition of receptors overexpressed on tumor cells[30-32]. Disappointingly, due to clinical trial results falling below expectations, active-targeting nanomedicines have not yet become available for clinical use[5,33-35]. The tumor-targeting failure of these nanotherapeutics could probably be traced to the impractical design of nanocarriers that ignored the complex *in vivo* microenvironments[36]. Particularly, emerging evidence suggests that the ligands modified on nanoparticles are often obscured by the formation of a protein corona in the bloodstream, severely blocking the recognition of targeting receptors[37,38]. As the existing strategies have failed to significantly improve drug accumulation in tumors, there is a growing expectation for the development of synergistic sensitization strategies to reduce chemotherapeutic thresholds[39]. The desired sensitization approach aims to selectively target and kill tumor cells while sparing normal cells. However, the risk of overlapping toxicity inevitably increases with multidrug combinations[40]. Given the existing deficiencies of both monotherapies and multidrug combinations, there's an urgent need to develop novel chemotherapeutic regimens with high efficiency and safety, ultimately unlocking the full potential of chemotherapy in clinical application.

Herein, we reported a self-sensitizing chemotherapeutic modality that enabled bidirectional therapeutic window expansion for chemotherapy (Fig. 1). Importantly, we were surprised to find that gossypol (GSP) greatly increased the sensitivity of cancer cells to several clinically available chemotherapeutics at previously ineffective concentrations, unlocking ultra-low-dose chemotherapeutic windows. Notably, since the concentration range of GSP used for chemotherapy sensitization elicited negligible effect on cell viability, it served as a chemotherapeutic booster instead of a secondary therapeutic drug. For proof-of-concept, cabazitaxel (CTX), a first-line chemotherapeutic drug with high activity and severe toxicity, was selected as the model drug to further explore the feasibility of GSP-aided chemotherapy. Significantly, GSP and CTX were found to readily co-aggregate into carrier-free binary nanoassemblies (NAs), which enabled the advantage of synchronous co-loading and co-delivery of the two compounds. Following optimization of the nanoassembly engineering, tumor-specific detachable PEG decoration on the NAs was implemented to achieve long blood circulation and tumor-specific drug release. As expected, the precisely engineered binary NAs displayed satisfactory therapeutic effects and favorable safety in prostate tumor-bearing C57BL/6 mouse models, even at a low CTX dose of 1 mg/kg. To our knowledge, this study represents the first endeavor to broaden the chemotherapeutic windows of CTX for prostate cancer treatment. This study drives a conceptual step forward in chemotherapeutic nanomedicines.

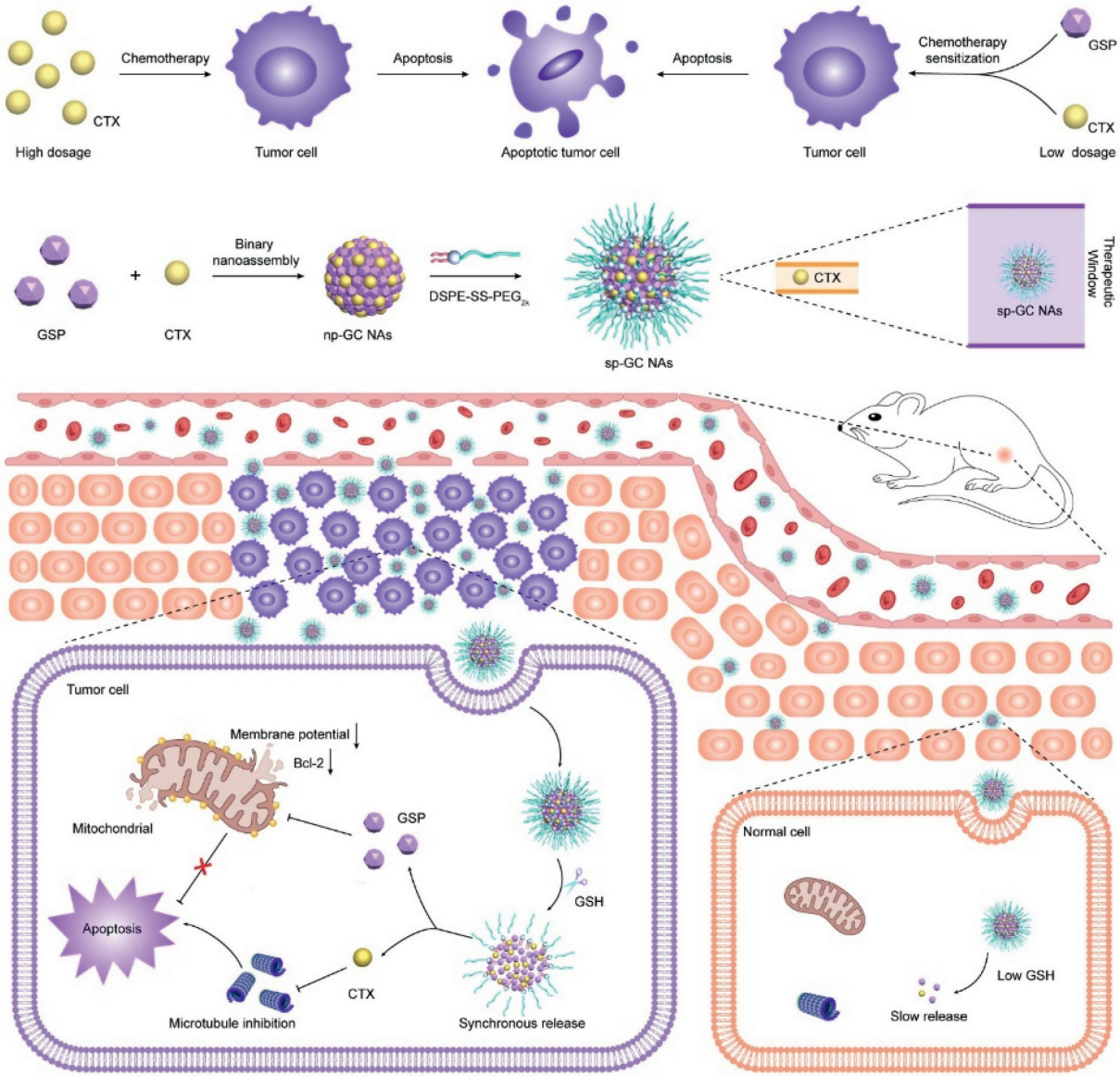

Figure 1 Schematic presentation of a natural chemotherapeutic enhancer-enabled therapeutic window broadening for prostate cancer treatment.

2. Materials and methods

2.1. Materials

Cabazitaxel (CTX), Cy7, trypsin-Ethylenediaminetetraacetic acid (trypsin−EDTA), Radio Immunoprecipitation Assay (RIPA)-lysis buffer, 3-(4,5-dimethyl-2-thiazolyl)-2,5-diphenyl-2*H*-tetrazolium bromide (MTT), EdU-488 cell proliferation detection kit, cell culture media and trypsin were purchased from Meilun Biotechnology Co., Ltd. (Dalian, China). Gossypol (GSP) was purchased from Macklin (Shanghai, China). DSPE-PEG_{2K}, Cy7-DSPE-PEG_{2K}, and Cy7-DSPE−SS−PEG_{2K} were purchased from Shanghai Advanced Vehicle Technology Co., Ltd. DSPE−SS−PEG_{2K} was obtained from Xi'an Ruixi Biological Technology Co., Ltd. The fetal bovine serum (FBS) and penicillin-streptomycin were purchased from GIBCO, Invitrogen Corp. (Carlsbad, California, USA). The antibodies were purchased from Abclonal Technology Co., Ltd. Annexin V-FITC/PI Apoptosis Detection Kit and Mitochondrial membrane potential test kit (JC-1) were purchased from Beijing Solarbio Science & Technology Co., Ltd. The living cell/dead cell staining kit was purchased from Shanghai Beibo Biotechnology Co., Ltd. Mouse testosterone ELISA kit was purchased from Shanghai ELISA Biotechnology Co., Ltd. Mitochondrial membrane potential detection Kit (JC-1) was purchased from Beijing Solarbio Science & Technology Co., Ltd. Hoechst 33342 was obtained from BD Biosciences (USA). Glass bottom cell culture dishes, cell culture dishes and plates were purchased from Wuxi NEST Biotechnology Co., Ltd., China. All other solvents mentioned in the article were of analytical grade or chromatographic grade.

2.2. Cell culture

The mouse breast tumor cell line (4T1 cells), mouse prostate cancer cell line (RM-1 cells), mouse fibroblast cell line (3T3 cells), and

human normal hepatic cell line (L02 cells) were obtained from the cell bank of the Chinese Academy of Sciences (Beijing, China). The 4T1 cells, RM-1 cells, and L02 cells were cultured with RPMI 1640 medium containing 10% FBS, streptomycin (100 units/mL), and penicillin (100 units/mL). The 3T3 cells were cultured in DMEM/F-12 medium with 10% FBS, streptomycin (100 units/mL), and penicillin (100 units/mL). All these cells were maintained in a humidified cell incubator (37 °C, 5% CO_2).

2.3. *In vitro GSP-sensitized cytotoxicity of multiple chemotherapeutics*

RM-1 cells, 4T1 cells, 3T3 cells, and L02 cells were used as cell models, respectively. MTT assay was used to compare the *in vitro* cytotoxicity of CTX and CTX/GSP (supplemented with 500 nmol/L GSP), DTX and DTX/GSP (supplemented with 500 nmol/L GSP), DOX and DOX/GSP (supplemented with 500 nmol/L GSP), OXP and OXP/GSP (supplemented with 500 nmol/L GSP), DDP and DDP/GSP (supplemented with 500 nmol/L GSP), as well as GEM and GEM/GSP (supplemented with 500 nmol/L GSP). In brief, cells (2×10^3 cells/well) were seeded into 96-well plates before drug treatment. After incubation for 12 h, the old culture medium was discarded, and the cells were exposed to serial dilutions of drug-containing media, respectively. After that, the culture was continued for 48 h in the incubator. At the end of the culture, 20 μL of MTT solution (5 mg/mL) was added to each well and cultured for another 4 h. Finally, the cell culture medium containing MTT was removed and 200 μL of DMSO was added. The 96-well plate was shaken in the oscillator for 10 min to fully dissolve formazan crystals, and the absorbance was measured at 492 nm by a microplate reader (ThermoFisher Scientific, USA). The median inhibition concentrations (IC_{50} values) were calculated by GraphPad Prism 8.0.

2.4. *Determination of the optimal formulation ratio of binary molecular nanoassembly*

The binary molecular nanoassembly was fabricated by a one-step nanoprecipitation method. The dose ratio was screened by analyzing and comparing the particle size (nm) and polydispersion index (PDI) of binary molecular nanoassemblies with different molar ratios. 2 mL of 0.5 mg/mL binary molecular nanoassemblies with different molar ratios (GSP: CTX = 20: 1-1: 10) were prepared. The particle size and PDI of the binary molecular nanoassembly were measured by a Malvern particle size analyzer.

MTT assay was used to investigate the cytotoxicity of binary molecular nanoassemblies with different molar ratios on tumor cells to further determine the optimal dose ratio. Using RM-1 cells and 4T1 cells as cell models, the prepared binary molecular nanoassemblies with different molar ratios (GSP: CTX = 20:1, 15:1, 10:1, 8:1, 6:1, 5:1, 3:1, 1:1) were diluted in a gradient according to the concentration of cabazitaxel, and then the drug-containing medium was co-incubated with RM-1 cells and 4T1 cells for 48 h, respectively. The other operations were the same as above. The median inhibition concentrations (IC_{50} values) were calculated by GraphPad Prism 8.0.

2.5. *Preparation and characterization of binary molecular nanoassembly*

The non-PEGylated binary molecular nanoassemblies (np-GC NAs) were fabricated by the one-step nanoprecipitation method. Briefly, CTX (2.00 mg) was dissolved in 400 μL of an ethanol/tetrahydrofuran mixture (1:1, *v*/*v*), and GSP (2.00 mg) was dissolved in 400 μL of the same mixed solvent. The mixtures of CTX and GSP at a molar ratio of 1:3 were obtained by taking 70 μL CTX reserve solution and 130 μL GSP reserve solution. Then, the mixed solutions were added dropwise into deionized water (2 mL) under robust stirring for 3 min. After that, the organic solvents in the nanosystems were removed by rotary evaporation at 30 °C to obtain a nanoassembly with a concentration of 0.5 mg/mL. Finally, the prepared nanoassembly was stored in the refrigerator at 4 °C. Additionally, the PEGylated binary molecular nanoassembly (p-GC NAs) and the SS-PEGylated binary molecular nanoassembly (sp-GC NAs) were constructed at the molar ratio of 1:3 (CTX/GSP) with a very similar procedure except for dropping DSPE-PEG_{2K} (30%, *w*/*w*) and DSPE−SS−PEG_{2K} (30%, *w*/*w*) into deionized water after dropping the CTX/GSP mixtures into deionized water.

To prepare Cy7-labeled PEGylated binary molecular nanoassembly and SS-PEGylated binary molecular nanoassembly for cellular uptake, biodistribution and pharmacokinetic study, DSPE-PEG_{2k} and DSPE−SS−PEG_{2k} labeled with Cy7 were used instead of DSPE-PEG_{2k} and DSPE−SS−PEG_{2k}. The preparation methods were the same as above.

The particle size, polydispersity index (PDI) and zeta potential of binary molecular nanoassembly were characterized by Zetasizer Nano ZS (Malvern, UK). The morphology of the binary molecular nanoassembly was observed by transmission electron microscopy (TEM, Hitachi, Japan). The TEM samples were prepared by dropping binary molecular nanoassembly solution on a 300-mesh carbon-coated copper grid and dried naturally, and then the 2% phosphotungstic acid was dropped on the carbon coated copper grid and dried thoroughly.

2.6. *Molecular co-assembly mechanisms*

The molecular interaction between CTX and GSP in the binary molecular nanoassembly was investigated using molecular docking simulation technology to explore the mechanism driving the assembly of the binary molecular nanoassembly. The chemical structures of CTX and GSP were converted into 3D structures, and subsequently, energy minimization conversion was carried out under the MFF94 force field. Finally, semi-flexible docking was performed using the AutoDock Vina program to output the optimal conformation and corresponding assembly forces.

At the same time, the Zetasizer Nano ZS (Malvern, UK) was used to determine the diameters of the binary molecular nanoassembly after incubation with sodium dodecyl sulfate (SDS, 50 mmol/L), sodium chloride (NaCl, 50 mmol/L) and urea (50 mmol/L), to further verify the intermolecular forces driving the assembly of the binary molecular nanoassembly.

2.7. *Stability*

The colloidal stability of the binary molecular nanoassembly was investigated by monitoring the particle size change. Briefly, 1 mL of np-GC NAs, p-GC NAs or sp-GC NAs was injected into 19 mL of phosphate buffer solution (PBS, pH 7.4) and incubated in a constant temperature shaker at 37 °C (100 rpm). At predetermined times (0, 0.0167, 0.5, 1, 2, 4, 6, 8, 12 and 24 h), the particle size changes of the binary molecular nanoassembly were determined by Zetasizer Nano ZS (Malvern, UK). To further investigate the stability of np-GC NAs, p-GC NAs and sp-GC NAs under

simulated physiological conditions, 10% FBS (*v/v*) was added to PBS (pH 7.4), and the remaining procedures were as above.

The np-GC NAs, p-GC NAs, and sp-GC NAs at concentrations of 1 mg/mL were stored in a refrigerator at 4 °C and kept out of light. The particle sizes of the np-GC NAs, p-GC NAs, and sp-GC NAs were measured at predetermined times (Days 0, 1, 2, 4, 6, 8 11, and 26), respectively.

2.8. *In vitro drug release*

The *in vitro* drug release behavior of CTX and GSP from the binary molecular nanoassembly in the presence or absence of DTT (5 mmol/L) was investigated by high-performance liquid chromatography (HPLC). Since both CTX and GSP were hydrophobic molecules, PBS (pH 7.4) containing 20% tetrahydrofuran (THF) was used to solubilize them. Briefly, 0.5 mL of 1 mg/mL of p-GC NAs or sp-GC NAs were added to dialysis bags, and the dialysis bags were immersed in 30 mL of PBS solution containing 20% THF in the presence (5 mmol/L) or absence (0 mmol/L) of DTT, and the mixture was placed in a constant temperature shaker (100 rpm) at 37 °C. At presupposed time points (0, 0.05, 1, 2, 4, 6, 8, and 12 h), 200 μL of release medium was taken out and the same volume of medium was added to the conical flask. HPLC determined the accumulative release of CTX and GSP from p-GC NAs or sp-GC NAs. The chromatographic separation conditions: C18 chromatographic column (4.6 mm × 250 mm, 5 μm); CTX: Mobile phase A: methanol, 80%; Mobile phase B: deionized water; GSP: Mobile phase A: methanol, 90%; Mobile phase B: deionized water containing 2‰ phosphoric acid, 10%. The flow rate was 1.0 mL/min, and the test wavelength of CTX and GSP was 230 nm.

2.9. *Cellular uptake*

The cellular uptake behavior of the binary molecular nanoassembly was investigated in RM-1 cells. Briefly, RM-1 cells were seeded in 24-well plates (5×10^4 cells/well). After incubation for 12 h, the original culture medium was discarded, 1 mL of fresh culture medium containing Cy7 Sol, Cy7-p-GC NAs, and Cy7-sp-GC NAs (200 ng/mL, Cy7 equivalent) was added to each well, and the cells were cultured for 0.5 and 4 h, respectively. Then, the drug-containing medium were removed and cellular uptake was stopped with ice-cold PBS. Subsequently, RM-1 cells were fixed with 4% paraformaldehyde for 10 min and washed three times with PBS. Thereafter, the nuclei were stained with Hoechst 33342 and washed three times with PBS. Finally, the intracellular fluorescence signals were observed by confocal laser scanning microscopy (CLSM, C2, Nikon, Japan). RM-1 cells without any treatment were used as controls.

For quantitative evaluation of cellular uptake, RM-1 cells were seeded into 12-well plates (2×10^5 cells/well) for 12 h. The dose concentration and incubation process were the same as above. At the end of incubation, the drug-containing medium was discarded, and ice-cold PBS was used to stop cellular uptake and wash away the remaining drug. The cells were separated and collected after treatment with trypsin, and resuspended in PBS. The intracellular fluorescence signals were estimated by the FACSCalibur flow cytometer (BD, USA).

2.10. *Cytotoxicity*

The cytotoxicity of the binary molecular nanoassembly against RM-1 cells, 4T1 cells, 3T3 cells, and L02 cells was measured by MTT assay. Briefly, cells in 96-well plates (2000 cells/well) were cultured in a cell incubator (37 °C, 5% CO_2) for 12 h. Then the original cell culture medium was replaced with a fresh culture medium containing a series of concentrations of CTX, GC, p-GC NAs, and sp-GC NAs, and sequentially cultured for 48 h. The cells without any treatment were used as control. The other operations were the same as in section 2.3.

2.11. *Live/dead cell co-staining*

The co-staining of live/dead cells treated with the binary molecular nanoassembly against RM-1 cells was investigated by laser confocal microscopy. In brief, RM-1 cells were seeded in 24-well glass bottom dishes covered with coverslips and cultured for 12 h (5×10^4 cells/well). Then, the old medium was discarded, and the cells were cultured with fresh medium containing CTX, GSP, GC, p-GC NAs, and sp-GC NAs (100 nmol/L, CTX equivalent, and/or 300 nmol/L, GSP equivalent) for 24 h, respectively. After that, the drug-containing media were removed, and the cells were washed three times with PBS. Subsequently, the cells were stained with Calcein-AM and PI for 30 min respectively and washed with PBS. Finally, the cellular fluorescence was observed by confocal laser scanning microscopy (CLSM, C2, Nikon, Japan). The cells without any treatment were used as controls.

2.12. *Apoptosis assay*

The apoptosis of RM-1 cells treated with the binary molecular nanoassembly was investigated by flow cytometry. In short, RM-1 cells were seeded in a 12-well glass bottom dish and cultured for 12 h (2×10^5 cells/well). Then, the old medium was discarded, and the cells were cultured with fresh medium containing CTX, GSP, GC, p-GC NAs and sp-GC NAs (100 nmol/L, CTX equivalent and/or 300 nmol/L, GSP equivalent) for 24 h, respectively. After that, the old cell culture medium was collected into a centrifuge tube, and the cells were digested with trypsin without EDTA. Subsequently, the digestion was terminated with the old culture medium, and the cells were gently blown down and dispersed. Thereafter, the cells were collected into the centrifuge tube again, the supernatant was removed by centrifugation at low temperature, the cells were washed with cold PBS, and the cells were resuspended with 100 μL of 1 × Binding Buffer. Finally, 5 μL of Annexin V/FITC was added and incubated in the dark for 5 min, later on, 5 μL pyridine iodide solution (PI) and 1 × Binding Buffer (400 μL) were added successively. The intracellular fluorescence signals were estimated by the FACSCalibur flow cytometer (BD, USA). The cells without any treatment were used as controls.

2.13. *EdU assay for analyzing cell proliferation*

The cell proliferation treated with the binary molecular nanoassembly against RM-1 cells was determined with EdU assay using Meilun EdU Cell Proliferation Kit with Alexa Fluor 488 according to the manufacturer's protocol. The same procedure for cell culture and administration as in section 2.12 was followed. At the end of incubation, an EdU working solution was added for EdU labeling, and the cells were fixed at room temperature for 15 min, followed by cell permeation for 10 min. Click reaction solution was added and incubated at room temperature for 30 min in the dark. Then the nuclei were labeled with Hoechst 33342 solution. Finally, the proliferation of antitumor cells was observed by confocal microscopy.

For the quantitative evaluation of cell proliferation, the basic operation was the same as above. Briefly, RM-1 cells were seeded into 24-well plates (5×10^4 cells/well) for 12 h. After EdU labeling was completed, the cells were digested with trypsin and transferred to a 1.5 mL EP tube. The supernatant was removed by centrifugation at low temperature for 5 min (1000 rpm, 4 °C), and no staining with 1 × Hoechst 33342 solution was required. The cells were resuspended with 500 μL wash solution, filtered through a 70 μm cell filter membrane, and then added to flow cytometry. Quantitative observation of antitumor cell proliferation was conducted by flow cytometry. The cells without any treatment were used as controls.

2.14. Western blotting

RM-1 cells were seeded into cell culture dishes (2×10^6 cells/well) for 12 h. Then, the old medium was discarded, and the cells were cultured with fresh medium containing CTX, GSP, GC, p-GC NAs, and sp-GC NAs for 40 h (10 nmol/L, CTX equivalent and/or 30 nmol/L, GSP equivalent), respectively. The cells without any treatment were used as controls. At the end of the culture, the cells were washed twice with cold PBS and collected. After centrifugation at low temperature for 5 min (1000 rpm, 4 °C), the supernatant was removed, and 150 μL of RIPA lysate was added for lysis for 15 min. After centrifugation, the supernatant protein solution was taken for quantification by the BCA colorimetric method, and 5 × protein supernatant dilution was added to the supernatant. Boil for 10 min. Proteins were isolated with 10% protein preform gel (10 wells, Tris-Gly, 1.0 mm), and the protein bands were transferred to PVDF membranes and blocked with 5% milk for 1 h. The protein bands were incubated overnight with corresponding primary antibodies Bcl-2, Bax, Pro-Caspase 3, and β-Actin in a refrigerator at 4 °C. After incubation, the non-specifically bound primary antibody liquid was washed with 1 × TBST, and the corresponding secondary antibody was incubated at 37 °C for 1 h. The membrane was washed and developed with a hypersensitive ECL solution.

2.15. Mitochondrial membrane potential assay

The mitochondrial membrane potential of RM-1 cells treated with binary molecular nano-assembly was studied using confocal and flow cytometry. The cell culture and administration procedures were the same as in Section 4.12. Old cell cultures were collected into centrifuge tubes and 1 mL of cell culture solution was added, followed by 1 mL of JC-1 staining working solution, which was mixed thoroughly and incubated in a cell culture incubator at 37 °C for 20 min. When the incubation was finished, the supernatant was aspirated and washed twice with cold JC-1 buffer. Finally, the mitochondrial membrane potential of the cells was observed by confocal microscopy. Cells without any treatment were used as controls.

For quantitative evaluation of mitochondrial membrane potential, the basic procedure was the same. Briefly, RM-1 cells were inoculated in 12-well plates (5×10^4 cells/well) for 12 h. At the end of the administration incubation, cells were digested with trypsin and transferred to 1.5 mL EP tubes. The supernatant was centrifuged at low temperature for 5 min (1000 rpm, 4 °C), followed by the addition of 0.5 mL of cell culture medium to resuspend the cells, and then 0.5 mL of JC-1 staining working solution, The rest of the operation was performed as above. Finally, mitochondrial membrane potential was quantified by flow cytometry. Cells without any treatment were used as controls.

2.16. Mitochondrial permeability transition pore (MPTP) assay

The mitochondrial permeability transition pore (MPTP) of RM-1 cells treated with binary molecular nano-assembly was studied using confocal and flow cytometry. The cell culture and administration procedures were the same as in Section 4.12. The culture solution was aspirated, and the cells were washed twice with PBS. Add 250 μL of Calcein AM Staining Solution, Fluorescence Quenching Solution or Ionomycin Control and shake gently so that the dye covers all cells evenly. Subsequently, the cells were incubated at 37 °C for 30 min. At the end of the incubation, the culture medium was replaced with fresh pre-warmed culture medium at 37 °C and incubated at 37 °C for another 30 min to ensure that the intracellular esterase fully hydrolyzed Calcein AM to produce green fluorescent Calcein. The culture medium was then aspirated, washed twice with PBS, and the cells were subsequently stained for 10 min with Hoechst 33342 Live Cell Staining Solution, washed twice with PBS, and finally the mitochondrial permeability transition pore opening of the cells was observed by confocal microscopy. Cells without any treatment were used as controls.

For quantitative evaluation of mitochondrial permeability transition pore opening, the basic procedure was the same as above. Briefly, RM-1 cells were inoculated in 12-well plates (5×10^4 cells/well) for 12 h. At the end of the administered incubation, cells were digested with trypsin and transferred to 1.5 mL EP tubes. The supernatant was centrifuged at low temperature for 5 min (1000 rpm, 4 °C), and the cells were resuspended by adding 1 mL of cell culture medium. The rest of the procedure was performed as above. Finally, mitochondrial permeability transition pore opening was quantified by flow cytometry. Cells without any treatment were used as controls.

2.17. Animal studies

Sprague−Dawley (SD) rats and C57BL/6 mice were supplied by the Animal Centre of Shenyang Pharmaceutical University (Shenyang, China). The use of animals was approved by the Animal Ethics Committee of Shenyang Pharmaceutical University (No.19169). All animal procedures were performed in accordance with the Guidelines for Care and Use of Laboratory Animals of Shenyang Pharmaceutical University and approved by the Animal Ethics Committee of Shenyang Pharmaceutical University.

2.18. Pharmacokinetics

Sprague−Dawley (SD) rats (200−220 g) were randomly divided into three groups to study the pharmacokinetic behavior of the binary molecular nanoassembly *in vivo* ($n = 6$). Cy7 Sol, Cy7-p-GC NAs, and Cy7-sp-GC NAs (2 mg/kg, Cy7 equivalent) were injected into the tail vein of rats, respectively. After intravenous injection, blood was collected from the ophthalmic vein of rats at predetermined time points at 0.033, 0.083, 0.25, 0.5, 1, 2, 4, 8 and 12 h. The plasma was obtained *via* centrifugation (8000 rpm, 3 min). The plasma concentrations of Cy7 were determined by a microplate reader (ThermoFisher Scientific, USA) at EX 744 nm and EM 776 nm.

2.19. Biodistribution

The *in vivo* biodistribution of binary molecular nanoassembly was investigated using the RM-1 prostate tumor-bearing C57BL/6

mice model ($n = 3$). To establish the tumor-bearing mice model, 100 μL of PBS containing RM-1 cells (5×10^6 cells) was inoculated subcutaneously into the right rear flank of male C57BL/6 mice. Once the tumor volume reached about 400 mm^3, Cy7 Sol, Cy7-p-GC NAs, and Cy7-sp-GC NAs (2 mg/kg, Cy7 equivalent) were injected into the tail vein, respectively. Fluorescence imaging was performed at 2, 4, 8, 16, and 24 h post-injection using a small-animal *in vivo* imaging system (PerkinElmer, IVIS spectrum, USA). Finally, the mice were euthanized at 4 h, the time point when the fluorescence intensity at the tumor site was the strongest *in vivo* imaging. The main organs (heart, liver, spleen, lung and kidney) and tumors of the mice were isolated and harvested for fluorescence imaging.

2.20. *In vivo antitumor efficacy*

The *in vivo* antitumor efficacy of the binary molecular nanoassembly was evaluated using the RM-1 prostate tumor-bearing C57BL/6 mice model. The establishment method for the tumor-bearing mice model was similar to section 4.19. Once the tumor volume reached approximately 100 mm^3, the mice were randomly divided into 6 groups ($n = 5$). The mice were administered with saline, CTX Sol, GSP Sol, GC Sol, p-GC NAs, and sp-GC NAs (4 mg/kg, CTX equivalent and/or 7.5 mg/kg, GSP equivalent) three times every 3 days. Tumor volume and body weight of the tumor-bearing C57BL/6 mice were measured and recorded daily. Two days after the last administration, all tumor-bearing C57BL/6 mice were weighed and sacrificed, and the heart, liver, spleen, lung, kidney and tumor tissues of the mice were isolated and obtained. Subsequently, the obtained tumor tissues were photographed and weighed, then the main organs and tumors were fixed in a tissue fixative solution containing 4% paraformaldehyde. Wuhan Xavier Biotechnology Co., Ltd. was commissioned to slice and stain the tumor tissue sections and perform follow-up photographic scanning. The apoptosis and/or necrosis of tumor cells in tumor-bearing C57BL/6 mice in different treatment groups were evaluated by TUNEL and H&E staining. Untreated RM-1 prostate tumor-bearing C57BL/6 mice were used as controls.

2.21. *Western blotting of tumor tissue*

The sensitization mechanism of the binary molecular nanoassembly *in vivo* was verified by western blotting. The tumor tissues isolated from the pharmacodynamic evaluation were added into 300 μL RIPA lysate and treated by an ultrasonic cell shredder for 30 min. After centrifugation, the supernatant protein solution was taken and quantified by the BCA colorimetric method. 5 × protein loading dilution was added into the supernatant and boiled for 10 min. Western blotting was performed as in Section 4.14.

2.22. *Analysis of serum testosterone in tumor-bearing C57BL/6 mice*

The inhibition ability of the binary molecular nanoassembly on testosterone production was evaluated by measuring the serum testosterone content of tumor-bearing C57BL/6 mice. The experiment was carried out according to the instructions of the "Mouse Testosterone ELISA Assay Kit". Standard wells (50 μL standards of different concentrations), blank control wells (no sample and enzyme reagent, the other operations were the same), and sample wells were set respectively. First, 40 μL of sample dilution was added to the sample wells, followed by 10 μL of the sample. After gently stirring and mixing, 100 μL of enzyme reagent was added to each well and incubated at 37 °C for 60 min. Then, discard the liquid shake it dry, then fill each well with washing liquid. After that, add 50 μL of color developer A and then 50 μL of color developer B to each well, gently shaken, and kept away from light for 15 min at 37 °C. Finally, add 50 μL of stop solution per well to terminate the reaction. The absorbance of each well at 450 nm wavelength was measured by a microplate reader (ThermoFisher Scientific, USA).

2.23. *Hemolysis experiments assay*

Fresh blood was taken from the orbits of healthy SD rats, loaded into 1.5 mL centrifuge tubes containing heparin, and centrifuged (8000 rpm, 3 min) after shaking well to isolate the erythrocytes. The erythrocytes were separated by centrifugation (8000 rpm, 3 min). 50 μL of erythrocytes were taken and diluted to 1 mL with saline. Then 50 μL each of CTX Sol, GSP Sol, GC Sol, p-GC NAs, and sp-GC NAs were taken and added to the saline containing erythrocytes, and incubated at 37 °C for 3 h. Subsequently, the above samples were centrifuged at 10,000 rpm for 3 min. Finally, 200 μL of the supernatant was taken, and its UV absorption at 540 nm was measured by a multifunctional enzyme marker, with the saline group and the pure water group used as the negative and positive control group, respectively.

2.24. *GSP-rendered ultra-low-dose chemotherapeutic window in vivo*

GSP-rendered ultra-low-dose chemotherapeutic window *in vivo* was evaluated using an RM-1 prostate tumor-bearing C57BL/6 mice model. The establishment method for the tumor-bearing mice model was similar to Section 4.19. Once the tumor volume reached approximately 100 mm^3, the mice were randomly divided into 12 groups ($n = 5$), which were divided into group a (Saline), group b (CTX Sol_1: 1 mg/kg, CTX equivalent), group c (CTX Sol_2: 2 mg/kg, CTX equivalent), group d (CTX Sol_4: 4 mg/kg, CTX equivalent), group e (CTX Sol_6: 6 mg/kg, CTX equivalent), group f (CTX Sol_8: 8 mg/kg, CTX equivalent), group g (GSP Sol: 14.9 mg/kg, GSP equivalent), group h (sp-GC NAs_1: 1 mg/kg, CTX equivalent), group i (sp-GC NAs_2: 2 mg/kg, CTX equivalent), group j (sp-GC NAs_4: 4 mg/kg, CTX equivalent), group k (sp-GC NAs_6: 6 mg/kg, CTX equivalent) and group l (sp-GC NAs_8: 8 mg/kg, CTX equivalent). The tumor-bearing mice were intravenously administered every other day for a total of five injections. One day after the last administration, the orbital blood of mice was taken for a whole blood index test, and the rest of the pharmacodynamic evaluation procedures were the same as in Section 4.20.

2.25. *Statistical analysis*

All the data were calculated and presented as mean value ± standard deviation (SD). One-way analysis of variance (ANOVA) or Student's *t*-test was performed to analyze the statistical differences between comparative groups, and when P values were less than 0.05, differences were deemed statistically significant. Asterisks indicate $*P < 0.05$, $**P < 0.01$, $***P < 0.001$, $****P < 0.0001$, ns, not significant.

3. Results and discussion

3.1. Discovery of a natural chemotherapeutic booster

This project commenced with an interesting discovery that a natural compound (GSP) at ineffective doses significantly boosted the chemotherapy effectiveness of several clinically available drugs, including CTX, docetaxel (DTX), doxorubicin (DOX), oxaliplatin (OXP), cisplatin (DDP) and gemcitabine (GEM). As shown in Fig. 2A, GSP alone exerted almost no cytotoxicity against RM-1 mouse prostate cancer cells, 4T1 mouse breast cancer cells, 3T3 mouse embryonic fibroblast cells, and L02 human fetal hepatocytes, even at micromolar concentrations. Excitingly, GSP dramatically augmented the sensitivity of RM-1 cells to CTX, DTX, DOX OXP, DDP, and GEM at an ineffective concentration of 0.5 μmol/L (Fig. 2B−C and Supporting Information Figs. S1−S5). Particularly, the cytotoxicity of CTX against RM-1 cells (Fig. 2B and C) and 4T1 cells (Fig. 2D and E) was remarkably enhanced in the presence of GSP, resulting in a 100-fold or more reduction in IC_{50} values. More importantly, such a sensitizing effect was not observed in 3T3 and L02 cells under the same conditions. As shown in Fig. 2F−I, GSP had little effect on the cytotoxicity of CTX to these two normal cell lines. These results suggested that GSP was capable of selectively enhancing the chemotherapeutic sensitivity of tumor cells even at ineffective dose concentrations, making it a potential novel chemotherapeutic adjuvant to unlock new chemotherapy windows by sharply descending therapeutic thresholds.

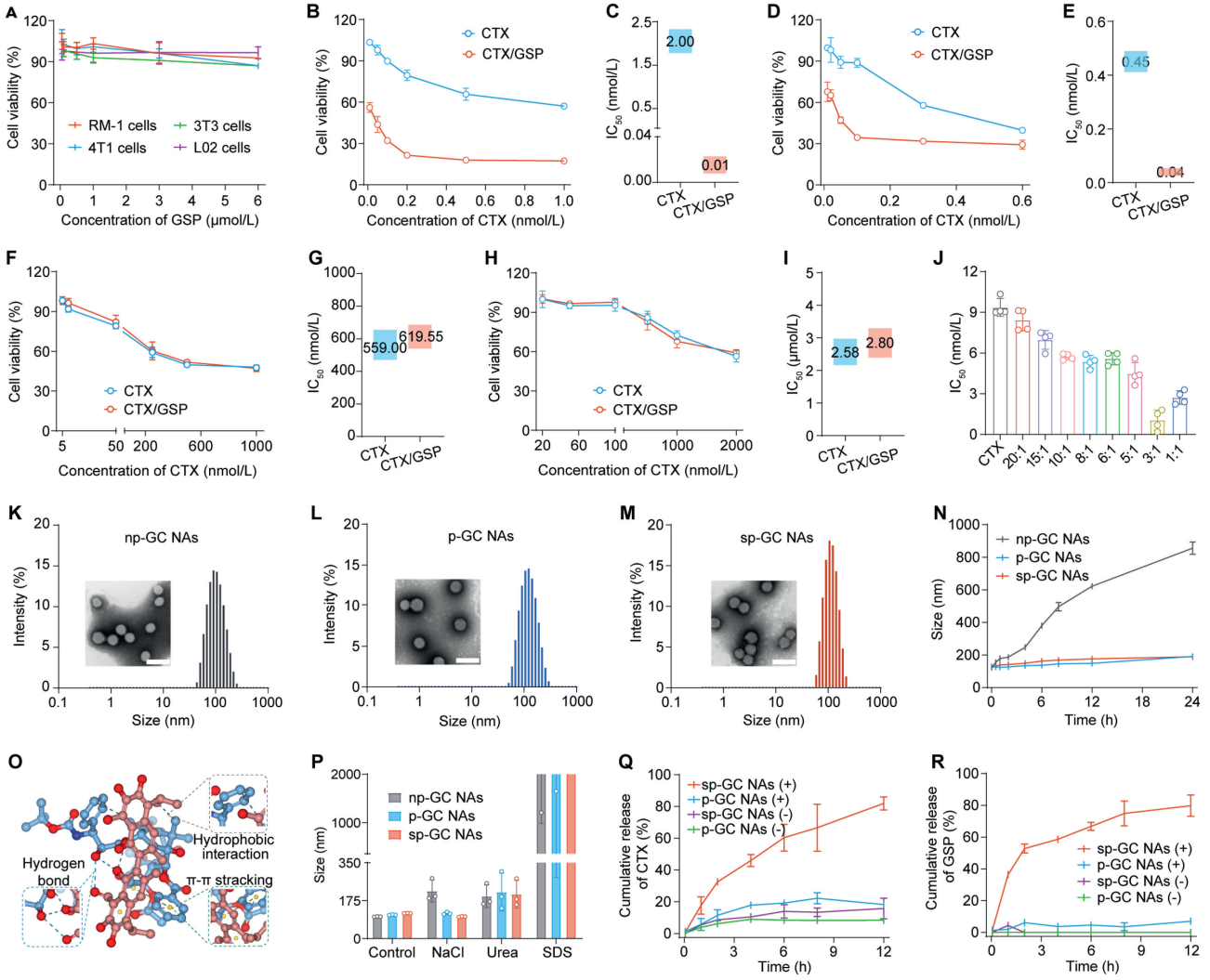

Figure 2 Discovery of a natural chemotherapeutic booster and elaborate fabrication of GSP/CTX binary nanoassembly. (A) Cytotoxicity of GSP against RM-1 cells, 4T1 cells, 3T3 cells and L02 cells. (B,C) Cytotoxicity of CTX and CTX/GSP against RM-1 cells. (D,E) Cytotoxicity of CTX and CTX/GSP against 4T1 cells. (F,G) Cytotoxicity of CTX and CTX/GSP against 3T3 cells. (H,I) Cytotoxicity of CTX and CTX/GSP against L02 cells. (J) IC_{50} values of GSP/CTX nanoassembly with different molar ratios against RM-1 cells. Data were presented as mean ± SD (n = 4). The size distribution and transmission electron microscope image of np-GC NAs (K), p-GC NAs (L) and sp-GC NAs (M). Scale bar = 200 nm. (N) The particle size changes of np-GC NAs, p-GC NAs and sp-GC NAs during incubation in PBS (pH 7.4). (O) Molecular docking simulation of CTX and GSP in binary nanoassembly. (P) The particle size changes of np-GC NAs, p-GC NAs and sp-GC NAs treated with Urea, SDS and NaCl (50 mmol/L), respectively. Cumulative release of CTX (Q) and GSP (R) from p-GC NAs and sp-GC NAs with (5 mmol/L) or without DTT for 12 h. Data were presented as mean ± SD (n = 3).

3.2. Elaborate fabrication of a carrier-free chemotherapeutic nano-booster

We found that GSP could co-assemble with CTX into carrier-free NAs in our previous attempts. Based on this, we proposed to develop a self-sensitive nanomedicine with a low-dose chemotherapeutic threshold. First, we intended to figure out the optimal GSP/CTX dose ratio when GSP served as a chemotherapeutic partner. The binary NAs were prepared at a range of molar GSP/CTX ratios from 20:1 to 1:10 by the one-step nanoprecipitation method. As shown in Supporting Information Table S1, GSP and CTX could readily co-assemble into carrier-free NAs with a wide GSP/CTX ratio range, spanning from 20:1 to 1:1 without the assistance of any excipients. A favorable co-assembly feature would certainly benefit efficient and synchronous delivery of GSP and CTX. Subsequently, the *in vitro* antitumor effects of GSP/CTX binary NAs were explored on RM-1 cells and 4T1 cells at different molar ratios. As shown in Fig. 2J and Supporting Information Fig. S6, the binary NAs with a GSP/CTX ratio of 3:1 presented the strongest cytotoxicity against both RM-1 and 4T1 cells within the molar ratio range from 20:1 to 1:1, resulting in minimum IC_{50} values of 0.64 nmol/L (RM-1 cells) and 0.23 nmol/L (4T1 cells), respectively. Fortunately, GSP and CTX at the optimal ratio (3:1) also demonstrated favorable nanoassembly performance (Table S1). Finally, a molar ratio of 3:1 (GSP/CTX) was selected as the optimal dose proportion for subsequent experiments.

PEGylation modification on carrier-free dual-drug NAs has proven to be an effective strategy to improve the colloidal stability and pharmacokinetic profiles[41,42]. Moreover, disulfide bond-containing prodrugs or polymeric materials have been extensively developed to achieve redox-responsive drug release triggered by the overproduction of glutathione (GSH) in tumor cells[11,42]. A small amount of disulfide bond-containing lipid-PEG (DSPE−SS−PEG_{2k}, 30 wt%) was used to fabricate redox-responsive GSP/CTX NAs (sp-GC NAs), which were expected to confer long blood circulation and tumor-specific release patterns of GSP and CTX. After optimizing the formulation, three nano-formulations were fabricated by one-step nano-precipitation method, including non-PEGylated, non-sensitive PEGylated, and redox-responsive PEGylated NAs. The non-PEGylated GSP/CTX NAs (np-GC NAs) were obtained through direct co-assembly of GSP and CTX. Meanwhile, the redox-responsive PEGylated GSP/CTX NAs (sp-GC NAs) and non-sensitive PEGylated GSP/CTX NAs (p-GC NAs) were prepared using DSPE−SS−PEG_{2k} and DSPE-PEG_{2k} as surface modifiers, respectively. Among them, np-GC NAs and p-GC NAs served as the non-PEGylated and non-sensitive control groups. As shown in Fig. 2K-M, Supporting Information Fig. S7 and Table S2, sp-GC NAs, np-GC NAs and p-GC NAs displayed uniform spherical nanostructures and appeared as yellow colloidal solutions with milky light, featuring favorable particle size (∼90−110 nm) and PDI (<0.2). Moreover, the PEGylated NAs (sp-GC NAs and p-GC NAs) exhibited slightly increased negative zeta potentials of ∼ −25 mV compared to the unmodified np-GC NAs (∼−6 mV), which would be conducive to the colloidal stability of NAs by preventing particle aggregation through charge repulsion. Negatively charged nanomedicines certainly benefit stability in the blood by preventing the interference by abundant plasma proteins. As shown in Fig. 2N and Supporting Information Fig. S8, the excellent nanoassembly performance of sp-GC NAs enabled good colloidal stability in both PBS (pH 7.4) and FBS-containing PBS (pH 7.4). By contrast, the non-PEGylated np-GC NAs showed poor stability under the same conditions. Moreover, these two PEGylated NAs (sp-GC NAs and p-GC NAs) showed favorable long-term stability at 4 °C, with no obvious changes in particle size (Supporting Information Fig. S9).

3.3. Nanoassembly mechanisms and drug release patterns

We then focused on the nanoassembly mechanisms and drug release patterns of binary NAs. First, we explored the nanoassembly mechanisms of the GSP/CTX pair. Molecular docking simulation technique was used to figure out the intermolecular forces. As illustrated in Fig. 2O, the nanoassembly of GSP and CTX was driven by a combination of π-π stacking force, hydrophobic interaction and hydrogen bonds. To verify these intermolecular forces, we employed sodium dodecyl sulfate (SDS), sodium chloride (NaCl), and urea as intermolecular force disruptors. As shown in Fig. 2P, a slight increase in the particle size of np-GC NAs was observed after incubation with NaCl for 3 h, while it had little impact on sp-GC NAs and p-GC NAs. These results indicated that electrostatic force promoted the nanoassembly of GSP and CTX, particularly under conditions without PEGylation decoration. Moreover, incubation with urea also elicited a slight increase in particle size increase in three NAs, suggesting the certain contribution of hydrogen bonding to GSP/CTX nanoassembly. Significantly, the particle sizes of the three binary NAs sharply increased in the presence of SDS, highlighting the dominant role of hydrophobic interactions in the co-assembly process of GSP and CTX.

As previously mentioned, DSPE−SS−PEG_{2k} decorated on sp-GC NAs was expected to trigger redox-responsive nanoassembly disintegration and drug release in tumor cells. We first investigated the morphological change of NAs after co-incubation with DTT. As shown in Supporting Information Fig. S10, the nanostructures of redox-responsive PEGylated sp-GC NAs were significantly destroyed, while those of non-sensitive PEGylated p-GC NAs remained intact spherical morphology. We then investigated the release patterns of GSP and CTX from sp-GC NAs and p-GC NAs in release media (pH 7.4) with or without DTT. Considering its poor stability, the bare np-GC NAs were excluded from subsequent studies. As shown in Fig. 2Q and R, both sp-GC NAs and p-GC NAs showed slow drug release in blank release media (pH 7.4, 0 mmol/L DTT), with less than 20% of GSP and CTX released. Notably, sp-GC NAs displayed DTT-triggered drug release features, with approximately 80% of GSP and CTX released in the presence of 5 mmol/L DTT within 12 h (Fig. 2Q and R). In contrast, the non-sensitive p-GC NAs revealed slow release even in a DTT-containing release medium. More significantly, the release profiles of CTX and GSP from sp-GC NPs were very similar in the presence of 5 mmol/L DTT within 12 h, displaying favorable and simultaneous drug release characteristics (Fig. 2Q and R). On-demand drug release from sp-GC NPs in the presence of DTT should be attributed to the inferior colloidal stability of sp-GC NAs after the loss of the PEG shell caused by reduction stimuli. In addition, the pH values of release media had little effect on drug release (Supporting Information Fig. S11). In the low pH release medium (pH 5.5 and 6.5) without the addition of DTT, both sp-GC NAs and p-GC NAs showed slow release, with less than 20% release within 12 h. The tumor-specific drug release pattern of sp-GC NAs would certainly benefit GSP-sensitized chemotherapy with low toxicity.

3.4. Cellular uptake

Given the critical role of cellular internalization in the therapeutic efficacy of nanomedicines, we further explored the cellular uptake efficiency of binary NAs in RM-1 cells. Cy7-labeled binary NAs (Cy7-p-GC NAs and Cy7-sp-GC NAs) were prepared to trace their cellular uptake characteristics, and the intracellular fluorescence signals of Cy7 were quantitatively and qualitatively detected by flow cytometry and laser confocal microscopy, respectively. As shown in Supporting Information Figs. S12 and 13, both Cy7-p-GC NAs and Cy7-sp-GC NAs exhibited higher intracellular fluorescence intensity than Cy7 Sol in a time-dependent manner, with no significant difference observed between the two NAs. The comparable cellular uptake efficiency of Cy7-p-GC NAs and Cy7-sp-GC NAs could be attributed to their very similar nanostructures, particle sizes, zeta potentials, and surface characteristics. These results indicated that binary NAs exhibited enhanced cellular uptake efficiency compared to free Cy7, likely due to a more efficient cellular internalization mechanism of nanomedicines through endocytosis[43].

3.5. Insight into GSP-mediated chemotherapy enhancement and mechanisms

The previous results demonstrated the sensitization effect of GSP on CTX-mediated chemotherapeutic cytotoxicity (Fig. 2B−E). Most importantly, such an adjuvant effect exhibited a notable advantage in terms of high selectivity between tumor cells and normal cells (Fig. 2F−I). We further expected that the redox-responsive drug release patterns of sp-GC NAs would further enhance the anticancer selectivity of CTX. To validate this hypothesis, we next evaluated the GSP-sensitized cytotoxicity of binary NAs in RM-1 and 4T1 cells using the MTT assay, with a specific focus on the underlying mechanisms. As shown in Fig. 3A and B, sp-GC NAs displayed the strongest cytotoxicity against both RM-1 cells and 4T1 cells compared to CTX Sol, GC Sol and non-sensitive p-GC NAs. In contrast, despite good stability and efficient cellular uptake, slow drug release from non-sensitive p-GC NAs led to inferior cytotoxicity (Fig. 3A and B), which once again underscored the crucial importance of rapid drug release in tumor cells for the therapeutic effects of nanomedicines. Notably, the mixed solution (GC Sol) only demonstrated a slight advantage over CTX Sol, which might be ascribed to the discrepant cellular uptake behaviors of CTX and GSP. As a result, GC Sol could not ensure an optimal synergy dose ratio, even if they were simultaneously exposed to RM-1 and 4T1 cells. These results suggested the necessity of synchronous and holistic drug delivery. Notably, both sp-GC NAs and p-GC NAs showed relatively weaker cytotoxicity in 3T3 and L02 cells compared to CTX Sol under the same conditions (Fig. 3C and D). It's easy to understand the slow drug release from non-sensitive p-GC NAs in both tumor and normal cells. Unlike tumor cells, lower redox levels in normal cells could also lead to inefficient drug release from sp-GC NAs, enabling favorable therapeutic selectivity between tumor and normal cells. Taken together, sp-GC NAs not only enhanced the anti-tumor effect through co-assembly with GSP but also provided desirable therapeutic selectivity due to tumor-specific drug release features. Such a self-sensitizing nanomedicine has the potential to serve as a novel chemotherapeutic modality for cancer treatment with high efficiency and safety.

Subsequently, the survival of RM-1 tumor cells after different treatments was investigated using the LIVE/DEAD Cell Imaging Kit. The living and dead cells were stained with calcein-AM (green) and propyl iodide (PI, red), respectively. As shown in Fig. 3E, only a small portion of cells treated with GSP Sol, CTX Sol, GC Sol, and p-GC NAs died, while strong red fluorescence signals were observed in sp-GC NAs, indicating a large number of cell deaths. This observation was consistent with the cell viability results (Fig. 3A and B). Meanwhile, we also detected the apoptosis proliferation of RM-1 cells after different treatments by flow cytometry and laser scanning confocal microscopy. Similar to the cell viability and live/dead cell staining results, the highest number of apoptotic cells was found in the sp-GC NAs group (>50%) compared to GSP Sol, CTX Sol, GC Sol, and p-GC NAs (Fig. 3F and Supporting Information Fig. S14). Moreover, EdU cell proliferation results also demonstrated the potent anti-proliferation activity of sp-GC NAs, with a significantly attenuated 488-Azid green fluorescence signal (Fig. 3G and H and Supporting Information Fig. S15). Taken together, these results suggested that sp-GC NAs exerted strong GSP-sensitized cytotoxicity through inhibiting cell proliferation and facilitating cell apoptosis. The potent cytotoxicity of sp-GC NAs should be attributed to its favorable stability, efficient cellular uptake, and redox stimuli-triggered rapid drug release features. These advantages of binary NAs cooperatively amplified the GSP-sensitized cytotoxicity of CTX.

We then investigated the underlying mechanisms of GSP-sensitized cytotoxicity of CTX. Growing evidence suggests that B-cell lymphoma-2 (Bcl-2) protein overexpressed in most tumor cells plays an anti-apoptotic role[8,44]. Moreover, the expression of Bcl-2 in tumor cells is usually upregulated upon exposure to chemotherapeutic drugs, leading to therapeutic resistance[45,46]. It has been reported that GSP can inhibit the cellular expression of Bcl-2 protein, up-regulate the expression of Bax, promote the activation of Caspase 3, and finally promote tumor cell apoptosis by the mitochondrial apoptosis pathway. We speculated that the sharply descended therapeutic threshold of CTX in the presence of GSP would be attributed to this cascade process (Fig. 4A). We first detected the expression of Bcl-2 protein in RM-1 cells after various treatments using a Western Blot assay. As shown in Fig. 4B, GSP-containing formulations (GSP Sol, GC Sol, and sp-GC NAs) except for the non-sensitive p-GC NAs significantly down-regulated the expression of Bcl-2, indicating that GSP effectively down-regulated Bcl-2 protein. The inferior Bcl-2 down-regulation effect of p-GC NAs should be ascribed to inefficient GSP release from the non-sensitive nanosystems (Fig. 2R). By contrast, sp-GC NAs with favorable stability, cellular uptake, and redox-responsive GSP release features remarkably suppressed Bcl-2 expression, resulting in GSP-sensitized cytotoxicity against tumor cells (Fig. 3A and B). Moreover, sp-GC NAs significantly up-regulated the expression of pro-apoptotic proteins Bax, which further led to the cleavage of pro-Caspase-3 (Supporting Information Fig. S17).

Mitochondrial membrane potential is closely related to cell apoptosis[47,48]. Subsequently, the mitochondrial membrane potential changes of RM-1 cells treated with different formulations were investigated using a mitochondrial membrane potential detection kit (JC-1). Cellular red (JC-1 aggregates) and green (JC-1 monomers) fluorescence represent high and low mitochondrial membrane potential, respectively. As shown in Fig. 4C−D and Fig. S14, strong red fluorescence signals were observed in the GSP Sol group and the untreated control group. The negligible impact of GSP alone on mitochondrial membrane potential should be ascribed to its weak cytotoxicity against RM-1 cells (Fig. 2B

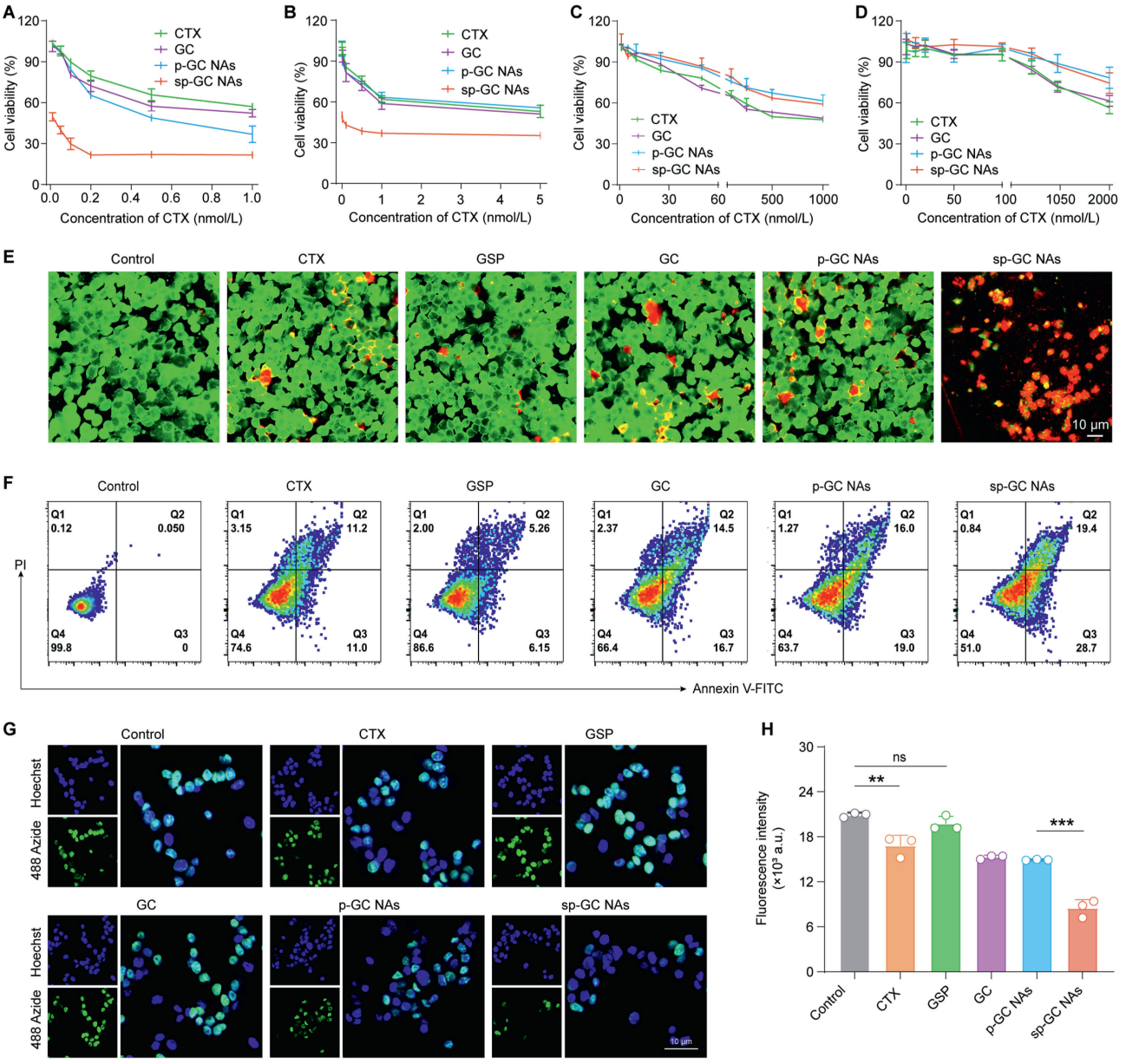

Figure 3 *In vitro* antitumor effects of GSP/CTX binary nanoassembly. (A) Cytotoxicity of CTX, GC, p-GC NAs, sp-GC NAs against RM-1 cells. (B) Cytotoxicity of CTX, GC, p-GC NAs, sp-GC NAs against 4T1 cells. (C) Cytotoxicity of CTX, GC, p-GC NAs, sp-GC NAs against 3T3 cells. (D) Cytotoxicity of CTX, GC, p-GC NAs, sp-GC NAs against L02 cells. Data were presented as mean ± SD ($n = 4$). (E) Live and dead cell co-staining assay. Confocal fluorescence images of CTX, GSP, GC, p-GC NAs or sp-GC NAs incubated with RM-1 cells. Cells were stained by Calcein-AM (live cell, green) and propidium iodide (dead cell, red). Scale bar = 10 μm. (F) The apoptosis and necrosis analysis of RM-1 cells stained by Annexin V-FITC and PI. (G) Cell proliferation assay. Confocal fluorescence images of CTX, GSP, GC, p-GC NAs or sp-GC NAs incubated with RM-1 cells. Proliferating cells were labeled with 488-Azide (green). Scale bar = 10 μm. (H) The cell proliferation analysis of RM-1 cells labeled by 488-Azide were quantified by flow cytometry. Data were presented as mean ± SD ($n = 3$). $^{**}P < 0.01$, $^{***}P < 0.001$, ns, not significant.

and C). By contrast, green fluorescence signals were significantly enhanced in RM-1 cells treated with CTX Sol compared with the untreated control group (Fig. 4C and D), indicating the apoptosis-promoting ability of CTX. Notably, much stronger green fluorescence signals were found in drug combination groups (GC Sol, p-GC NAs, and sp-GC NAs) than that observed in monotherapy of CTX and GSP (Fig. 4C and D), providing clear evidence of a synergistic sensitization effect between them. Among them, sp-GC NAs displayed distinct advantages over GC Sol and p-GC NAs in terms of mitochondrial membrane potential reduction (>75%), which can also be attributed to their favorable stability, cellular uptake, and redox-responsive GSP release features.

In addition, given the high correlation between cell apoptosis and the abnormal opening of the mitochondrial permeability transition pore (MPTP), we further explored the MPTP status of RM-1 cells after different treatments using the Calcein AM (Calcein acetoxymethyl ester) probe. The non-fluorescent Calcein AM can be readily converted to a fluorescent dye (Calcein)

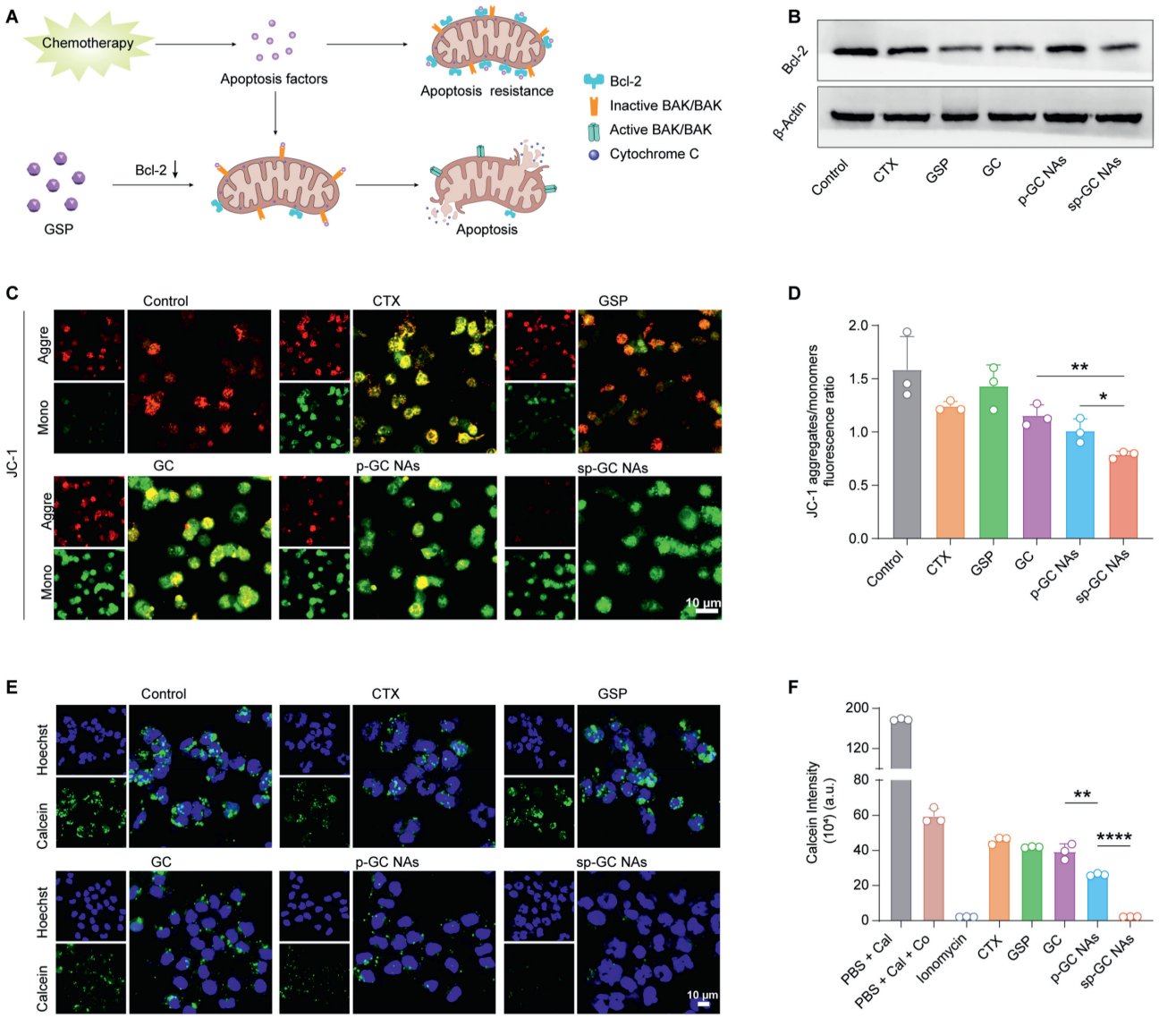

Figure 4 Insight into GSP-mediated adjuvant effect and mechanisms. (A) Schematic illustration of the mechanism of GSP-mediated adjuvant effect. (B) Western Blotting images of Bcl-2 protein expression in RM-1 cells. (C) The mitochondrial membrane potential analysis of RM-1 cells labeled with JC-1. Confocal fluorescence images of CTX, GSP, GC, p-GC NAs or sp-GC NAs incubated with RM-1 cells. JC-1 aggregates (red fluorescence), JC-1 monomers (green fluorescence). Scale bar = 10 μm. (D) Quantification of mitochondrial membrane potential depolarization by ImageJ. Ratio of fluorescence intensity of JC-1 aggregates to JC-1 monomers (red fluorescence intensity/green fluorescence intensity). (E) The mitochondrial permeability transition pore opening analysis of RM-1 cells labeled with Calcein AM. Confocal fluorescence images of CTX, GSP, GC, p-GC NAs or sp-GC NAs incubated with RM-1 cells. Scale bar = 10 μm. (F) The mitochondrial permeability transition pore opening analysis of RM-1 cells labeled with Calcein AM are quantified by flow cytometry. Data are presented as mean ± SD ($n = 3$). *$P < 0.05$, **$P < 0.01$ and ****$P < 0.0001$.

without membrane permeability, thus being trapped in mitochondria with strong green fluorescence[44,49]. Based on this principle, the degree of MPTP opening can be evaluated by detecting the Calcein green fluorescence signals in mitochondria. Stronger green fluorescence indicated a lower degree of MPTP opening. As shown in Fig. 4E and F, similar trends were observed in the MPTP changes as with the mitochondrial membrane potential. As expected, sp-GC NAs significantly elicited the abnormal opening of MPTP in RM-1 cells. Taken together, the self-sensitized cytotoxicity of sp-GC NAs should be ascribed to GSP-mediated Bcl-2 depletion and the synergistic triggering of mitochondrial dysfunction by GSP/CTX combo.

3.6. *Pharmacokinetics and biodistribution*

Satisfactory antitumor effects *in vivo* depend entirely on favorable pharmacokinetics and tumor-specific biodistribution. We expected that sp-GC NAs would leverage the hydrophilic coating of PEGylation to navigate the vasculature and accumulate at tumor sites *via* the enhanced permeability and retention (EPR) effect. Cy7-labeled NAs (Cy7-p-GC NAs and Cy7-sp-GC NAs) were prepared using Cy7-conjugated DSPE-PEG_{2k} as a PEGylation modifier. The pharmacokinetic profiles of NAs in rats were conveniently evaluated by detecting the fluorescence signals of Cy7. As shown in Supporting Information Fig. S18 and Table S3,

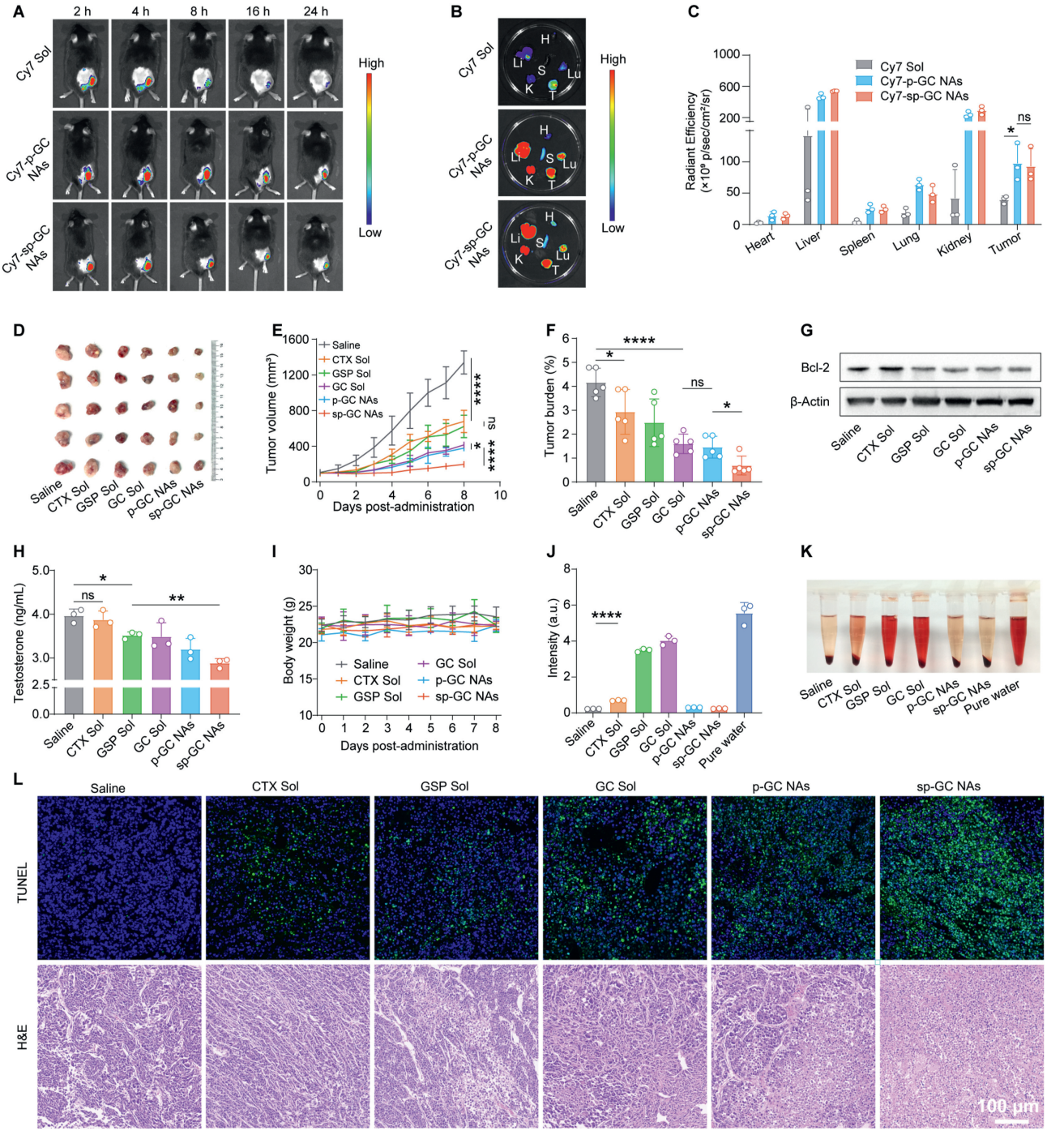

Figure 5 Tumor biodistribution and *in vivo* GSP-sensitized antitumor chemotherapy. (A) The living images of RM-1 tumor-bearing C57BL/6 mice treated with Cy7 Sol, Cy7-p-GC NAs and Cy7-sp-GC NAs at a Cy7 equivalent dose of 2 mg/kg. (B) *Ex vivo* fluorescent images of major organs and tumors at 4 h. (C) Quantitative results of major organs and tumors accumulation at 4 h. Data were presented as mean ± SD ($n = 3$). *$P < 0.05$, ns, not significant. (D) Images of tumors. (E) Tumor growth profiles treated with CTX Sol, GSP Sol, GC Sol, p-GC NAs or sp-GC NAs. (F) Tumor burden, the weight of tumors was divided by the average body weight of mice. (G) Western blotting results of Bcl-2 expression in tumor tissues. (H) The serum testosterone content of mice after various treatments was detected by mouse testosterone ELISA kit. (I) Body weight changes of mice bearing RM-1 tumor xenografts after treatment. Data were presented as mean ± SD ($n = 5$). *$P < 0.05$, **$P < 0.01$, ****$P < 0.0001$, ns, not significant. (J) Quantitative analysis of hemoglobin content of supernatant. Data were presented as mean ± SD ($n = 3$). ****$P < 0.0001$. (K) Hemolysis photograph. (L) H&E and TUNEL staining images of tumors after various treatments. Scale bar = 100 μm.

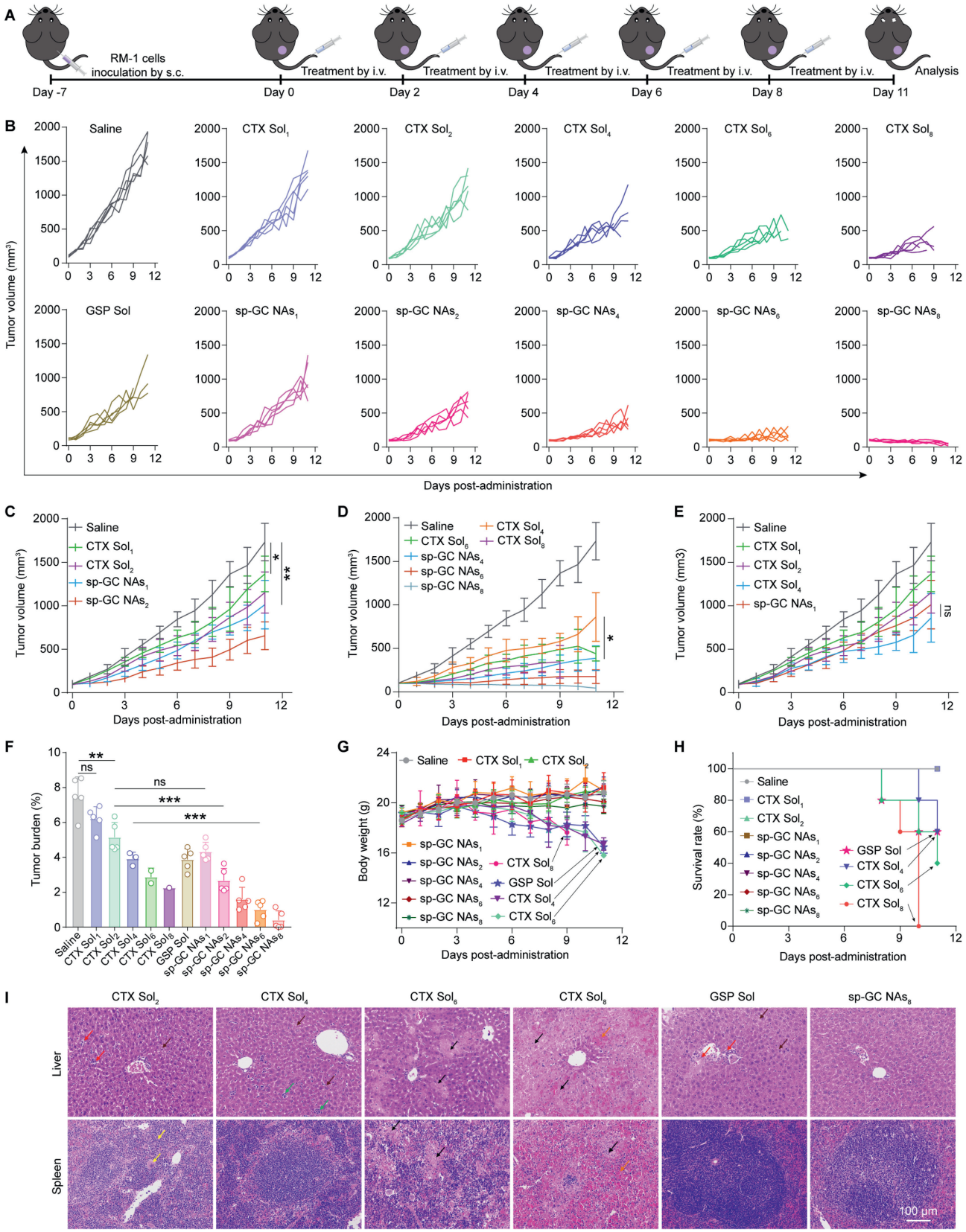

Figure 6 GSP-rendered chemotherapeutic window broadening *in vivo*. (A) Treatment schedule for chemotherapy. (B) Tumor growth profiles treated with different formulations. (C) Tumor growth profiles treated with Saline, CTX Sol_1, CTX Sol_2, sp-GC NAs_1 and sp-GC NAs_2 (subscripts 1 and 2 refer to equivalent CTX doses of 1 and 2 mg/kg, respectively). (D) Tumor growth profiles treated with Saline, CTX Sol_4, CTX Sol_6, CTX Sol_8, sp-GC NAs_4, sp-GC NAs_6 and sp-GC NAs_8 (subscripts 4, 6, and 8 refer to equivalent CTX doses of 4, 6, and 8 mg/kg, respectively).

Cy7 Sol was rapidly cleared from the blood with a short elimination half-life ($t_{1/2}$) of 1.6 ± 0.7 h. By contrast, the circulation time of Cy7-p-GC NAs and Cy7-sp-GC NAs in the blood was significantly prolonged, with their half-lives ($t_{1/2}$) increased by 2.3 times and 3.3 times compared to Cy7 Sol, respectively (Table S3). Meanwhile, Cy7-p-GC NAs and Cy7-sp-GC NAs displayed a larger area under the concentration−time curve (AUC) than Cy7 Sol. The favorable pharmacokinetic behaviors of NAs can be ascribed to the hydrophilic shell endowed by PEGylation decoration on both Cy7-p-GC NAs and Cy7-sp-GC NAs. Moreover, there was almost no significant difference between Cy7-p-GC NAs and Cy7-sp-GC NAs, possibly due to the similar surface characteristics of the two NAs.

The above pharmacokinetic results suggested that the favorable colloidal stability and PEGylation modification of Cy7-p-GC NAs and Cy7-sp-GC NAs dramatically improved *in vivo* drug delivery efficiency, which might favor drug accumulation at tumors *via* the EPR effect. We then evaluated the biodistribution of Cy7 Sol, Cy7-p-GC NAs, and Cy7-sp-GC NAs in a mouse RM-1 prostate cancer model. As shown in Fig. 5A−C, Cy7 Sol, Cy7-p-GC NAs and Cy7-sp-GC NAs in tumors reached the maximum accumulation at 4 h post-administration. The fluorescence signals of Cy7-p-GC NAs and Cy7-sp-GC NAs lasted at high intensity for 24 h. Notably, the fluorescence signals of Cy7 Sol in tumors were not only much weaker than those of Cy7-p-GC NAs and Cy7-sp-GC NAs at the maximum peak time point (4 h), but also rapidly decayed over time. The inferior tumor accumulation of Cy7 Sol can be attributed to its poor pharmacokinetic behavior (Fig. S18). Notably, the non-sensitive Cy7-p-GC NAs displayed certain advantages over Cy7-sp-GC NAs in terms of fluorescence signals in tumors, especially within the time range of 8 h−24 h. The non-sensitive feature led to better biodistribution performance of Cy7-p-GC NAs, while the stability of Cy7-sp-GC NAs got worse gradually with the disulfide bond breaking in the presence of GSH overproduced in tumor cells, resulting in quick clearance of the Cy7 probe. Therefore, although Cy7-p-GC NAs have a relatively higher biodistribution in tumors, slow drug release would be a major obstacle hindering antitumor therapy. By contrast, sp-GC NAs struck a better balance of colloidal stability, pharmacokinetics, tumor accumulation, and on-demand drug release, which was expected to achieve desirable GSP/CTX co-delivery and self-augmented chemotherapy.

3.7. GSP-sensitized antitumor chemotherapy

After elaborate engineering and characterization, a natural chemotherapeutic adjuvant-empowered nanoassembly (sp-GC NAs) with favorable drug delivery features was expected to significantly enhance CTX-elicited chemotherapy *in vivo*. A mouse RM-1 prostate cancer model was established to investigate GSP-sensitized chemotherapy of sp-GC NAs. CTX Sol, GSP Sol, GC Sol, p-GC NAs, and sp-GC NAs were intravenously administered to the tumor-bearing mice every three days for a total of three injections. The mice were sacrificed, and the main organs and tumors were obtained to explore therapeutic effects and mechanisms following the final treatment. As shown in Fig. 5D−F, owing to rapid elimination *in vivo* and inefficient tumor accumulation, monotherapy with GSP and CTX demonstrated moderate antitumor activity. By comparison, the mixture solution of GSP and CTX (GC Sol) and the non-sensitive p-GC NAs exerted more potent tumor growth inhibition than either GSP or CTX, indicating the GSP-sensitized antitumor effect of CTX. However, there was no significant difference between them. As previously discussed, despite the favorable pharmacokinetics and biodistribution results of p-GC NAs, slow drug release greatly confined the full exertion of GSP-sensitized chemotherapy. As expected, the redox-responsive binary nanoassembly (sp-GC NAs) almost completely suppressed tumor progression throughout the treatment process, which could be ascribed to the good stability, high cellular uptake, long blood circulation, efficient tumor accumulation, and on-demand release of GSP or CTX from the NAs in tumor cells.

We then verified the mechanisms of GSP-empowered chemotherapy adjuvant effects *in vivo*. We first analyzed the expression of Bcl-2 protein in tumor tissues by Western Blot assay after different treatments. As shown in Fig. 5G, sp-GC NAs significantly down-regulated the expression of Bcl-2 in tumor tissues, which was consistent with the *in vitro* results (Fig. 4B). In addition to Bcl-2 protein, increasing evidence indicates that androgens (*e.g.*, testosterone) play a key role in the occurrence and progression of prostate cancer[50]. Moreover, GSP has been reported to suppress prostate tumor growth by inhibiting the testosterone production of testicular stromal cells[51,52]. Based on this, we further explored the testosterone levels in mouse serum using mouse testosterone enzyme-linked immunoassay (ELISA) kit after different treatments. As shown in Fig. 5H, CTX alone elicited no change in serum testosterone. By contrast, the mice treated with GSP-containing formulations (GSP Sol, GC Sol, p-GC NAs, and sp-GC NAs) significantly showed a significant reduction in serum testosterone, especially in the sp-GC NAs group. Moreover, TUNEL and H&E staining results of tumor slices provided further evidence that sp-GC NAs could induce significant inhibition of cell proliferation (Fig. 5L). Additionally, no significant damage was caused by sp-GC NAs according to the body weight changes (Fig. 5I), hemolysis (Fig. 5J and K), H&E staining of the main organs (Supporting Information Fig. S19), and hepatorenal function parameters (Supporting Information Fig. S20). These results indicated that formulating GSP and CTX into sp-GC NAs not only exerted strong antitumor activity by down-regulating Bcl-2 expression in tumor tissues and inhibiting testosterone production but also exhibited good biocompatibility and biosafety.

(E) Tumor growth profiles treated with Saline, CTX Sol_1, CTX Sol_2, CTX Sol_4 and sp-GC NAs_1 (subscripts 1, 2, and 4 refer to equivalent CTX doses of 1, 2, and 4 mg/kg, respectively). (F) Tumor burden, the weight of tumors was divided by the average body weight of mice. (G) Body weight changes of mice bearing RM-1 tumor xenografts after treatment. (H) Survival rate of mice bearing RM-1 tumor xenografts after treatment. Data were presented as mean ± SD ($n = 5$). *$P < 0.05$, **$P < 0.01$, ***$P < 0.001$, ns, not significant. (I) H&E staining images of liver and spleen of mice bearing RM-1 tumor xenografts after the last treatments. Scale bar = 100 μm. Liver: brown arrow: cytoplasmic eosinophilic granules; red arrow: small focal infiltration of hepatic parenchymal lymphocytes; green arrow: small focal aggregates of extramedullary hematopoietic cells in the hepatic parenchyma; black arrow: large number of necrotic hepatocytes with fragmented nuclei and increased cytoplasmic eosinophilicity; orange arrow: associated with moderate hemorrhage. Spleen: black arrow: small focal necrosis, cytosolized nuclei, enhanced cytoplasmic eosinophilia; yellow arrow: small focal aggregates of giant cells; orange arrow: severe hemorrhage.

3.8. GSP-rendered chemotherapeutic window broadening in vivo

As previously discussed, sp-GC NAs were expected to uncover a new chemotherapeutic window for cancer treatment. To further validate the GSP-rendered chemotherapeutic window broadening *in vivo*, we conducted another pharmacodynamics experiment in RM-1 tumor-bearing C57BL/6 mice receiving CTX Sol or sp-GC NAs in a gradient from a low dose (1 mg/kg) to a high dose (8 mg/kg) of CTX, focusing simultaneously on tumor-suppressive effects and safety. The administration regimen was clearly shown in Fig. 6A, CTX Sol, and sp-GC NAs were intravenously administrated to the tumor-bearing mice every two days for a total of five injections at an equivalent CTX dose of 1, 2, 4, 6, and 8 mg/kg, respectively. As shown in Figs. 6B−H and Supporting Information Figs. S22 and S23, CTX Sol showed negligible anti-tumor effects at low doses (1 and 2 mg/kg), while it caused serious toxic side effects at high doses (4, 6 and 8 mg/kg), resulting in significant weight loss and even death of tumor-bearing mice. In contrast, sp-GC NAs not only displayed much stronger tumor inhibition effects than CTX Sol at low doses (1, 2 and 4 mg/kg) but also completely suppressed tumor growth at a high dose (8 mg/kg), with some tumors almost completely disappearing in mice. It was worth noting that sp-GC NAs still exhibited a good tumor inhibition effect at a dose of 1 mg/kg, which had obvious advantages over CTX Sol. Moreover, the TUNEL and H&E staining results further demonstrated the excellent inhibition effects of sp-GC NAs on tumor cell proliferation (Supporting Information Fig. S24). These results thoroughly verified the hypothesis that GSP unlocked an ultra-low-dose chemotherapeutic window for CTX.

In stark contrast with CTX Sol, sp-GC NAs displayed good safety in the dosage range of 1−8 mg/kg, no significant change in body weight, hepatorenal function and whole blood indexes were observed in any of the mouse populations (Fig. 6G and Supporting Information Figs. S25 and S26). By contrast, CTX Sol not only caused dramatic weight loss, but also led to abnormalities in hepatorenal function indicators and pancytopenia (Figs. S25 and 26). These results suggested that the integration of GSP and CTX not only dramatically descended the therapeutic threshold of CTX, but also greatly improved its maximum tolerable dose. In other words, a precise dual-drug nanoassembly of GSP and CTX rendered a bidirectional chemotherapeutic window extension for CTX, which would certainly confer better efficacy and safety to cancer chemotherapy. Furthermore, we also compared the antitumor efficacy and safety of GSP Sol with sp-GC NAs at an equivalent GSP dose of 14.9 mg/kg, which was the same GSP dose in sp-GC NAs at the high CTX dose of 8 mg/kg. As shown in Fig. 6B and G, GSP Sol had only moderate antitumor effects, but the body weight of tumor-bearing mice decreased significantly at a high dose. Moreover, some degree of liver injury was found in liver tissue sections (Fig. 6I and Supporting Information Figs. S27 and S28). Obviously, GSP Sol not only showed poor anti-tumor activity even at high doses but might also cause liver damage. By contrast, formulating it into a GSP/CTX binary nanoassembly (sp-GC NAs) significantly sensitized CTX-mediated chemotherapy while significantly attenuating off-target toxicity at the same dose of GSP, which should be ascribed to on-demand drug release in the presence of redox stimuli in tumors (Fig. 2Q and R). These results indicate that sp-GC NAs significantly broadened the therapeutic window of CTX by virtue of the GSP-mediated chemotherapy adjuvant effect, rendering an ultra-low-dose therapeutic threshold and a high tolerance dose.

4. Conclusions

To enhance the sensitivity of chemotherapy for prostate cancer, we proposed the concept of exploiting a self-sensitized nano-booster integrated with a tumor-specific chemotherapeutic enhancer, enabling therapeutic window expansion and efficacy-toxicity benefit amplification in prostate cancer treatment. We have identified and explored the feasibility of using a natural chemotherapeutic enhancer to broaden the therapeutic window for effective prostate cancer chemotherapy. The nanoassembly formulation (sp-GC NAs) was based on molecular co-assembly nanotechnology, comprising GSP, CTX, and DSPE−SS−PEG_{2k}. Unlike conventional polymeric nanomedicines, sp-GC NAs were molecularly self-aggregated nanoassemblies of two small molecular drugs (GSP and CTX). The main framework of sp-GC NAs was formed through the co-assembly of GSP and CTX, rather than relying on DSPE−SS−PEG_{2k}. GSP and CTX co-assembled into uniform nanostructures without the assistance of any carrier material. In this context, DSPE−SS−PEG_{2k} performed as a PEGylation modifier rather than a carrier material in sp-GC NAs. Furthermore, as a disulfide bond-containing lipid-PEG, DSPE−SS−PEG_{2k} plays a crucial role in achieving redox-responsive release of GSP and CTX in tumor cells with an overproduction of GSH. Crucially, by virtue of the advantages of small-molecule drug nanoassembly techniques, sp-GC NAs exhibited excellent drug co-loading capacity (70%) for GSP and CTX.

Formulating GSP and CTX into a redox-responsive nanoassembly enabled desirable drug co-delivery and on-demand drug release. We further showed that the GSP/CTX binary NAs not only unlocked an ultra-low-dose chemotherapeutic window by significantly lowering the therapeutic threshold of CTX at ineffective dose concentrations of GSP, but also greatly improved the tolerable dose of CTX through precise dual-drug nanoassembly. More importantly, the GSP-mediated chemotherapy adjuvant effect demonstrated remarkable selectivity between normal and tumor cells, enabling an ideal anticancer modality against prostate cancer. The nano-booster displayed potent antitumor activity in mouse prostate tumor xenograft models, even at a low CTX dose of 1 mg/kg. Safety evaluations suggested that sp-GC NAs did not induce weight loss, hepatic or renal function impairment, or pathological tissue changes during the treatment period. The therapeutic safety of sp-GC NAs can be attributed to redox-responsive PEGylation modification and the high selectivity of their synergistic action against prostate cancer cells. These findings presented a fresh perspective for revisiting the importance and potential of chemotherapy, opening up possibilities for the development of a new generation of chemotherapeutic nanomedicines with good clinical applicability.

Acknowledgments

This work was financially supported by the National Natural Science Foundation of China (No. 82161138029), the Basic Research Projects of Liaoning Provincial Department of Education (LJKZZ20220109, China), and the Shenyang Youth Science and Technology Innovation Talents Program (No. RC210452,

China). We would like to acknowledge the excellent technical support provided by the Animal Ethics Committee of Shenyang Pharmaceutical University.

Author contributions

Rui Liao: Writing − original draft, Investigation, Formal analysis, Data curation. Yuequan Wang: Writing − original draft, Methodology, Investigation, Data curation. Ziqi Lin: Methodology, Investigation, Formal analysis, Data curation. Yuting Wang: Validation, Software, Methodology. Hongyuan Zhang: Validation, Resources. Qin Chen: Validation, Supervision, Project administration. Shenwu Zhang: Visualization, Supervision, Project administration. Jin Sun: Visualization, Conceptualization. Zhonggui He: Supervision, Project administration, Conceptualization. Cong Luo: Writing − review & editing, Writing − original draft, Visualization, Project administration, Funding acquisition, Conceptualization.

Conflicts of interest

The authors declare no conflicts of interests.

Appendix A. Supporting information

Supporting information to this article can be found online at https://doi.org/10.1016/j.apsb.2025.03.029.

References

1. Miller KD, Nogueira L, Devasia T, Mariotto AB, Yabroff KR, Jemal A, et al. Cancer treatment and survivorship statistics, 2022. *CA Cancer J Clin* 2022;**72**:409−36.
2. Siegel RL, Miller KD, Wagle NS, Jemal A. Cancer statistics, 2023. *CA Cancer J Clin* 2023;**73**:17−48.
3. Chow A, Perica K, Klebanoff CA, Wolchok JD. Clinical implications of T cell exhaustion for cancer immunotherapy. *Nat Rev Clin Oncol* 2022;**19**:775−90.
4. Passaro A, Brahmer J, Antonia S, Mok T, Peters S. Managing resistance to immune checkpoint inhibitors in lung cancer: treatment and novel strategies. *J Clin Oncol* 2022;**40**:598−610.
5. Lahiri A, Maji A, Potdar PD, Singh N, Parikh P, Bisht B, et al. Lung cancer immunotherapy: progress, pitfalls, and promises. *Mol Cancer* 2023;**22**:40.
6. Afzal M, Ameeduzzafar Alharbi KS, Alruwaili NK, Al-Abassi FA, Al-Malki AAL, et al. Nanomedicine in treatment of breast cancer—a challenge to conventional therapy. *Semin Cancer Biol* 2021;**69**: 279−92.
7. Labrie M, Brugge JS, Mills GB, Zervantonakis IK. Therapy resistance: opportunities created by adaptive responses to targeted therapies in cancer. *Nat Rev Cancer* 2022;**22**:323−39.
8. Hanahan D, Weinberg RA. Hallmarks of cancer: the next generation. *Cell* 2011;**144**:646−74.
9. Vesely MD, Zhang T, Chen L. Resistance mechanisms to anti-PD cancer immunotherapy. *Annu Rev Immunol* 2022;**40**:45−74.
10. Yadav D, Kwak M, Chauhan PS, Puranik N, Lee PCW, Jin JO. Cancer immunotherapy by immune checkpoint blockade and its advanced application using bio-nanomaterials. *Semin Cancer Biol* 2022;**86**: 909−22.
11. Sun XX, Yang XH, Wang J, Shang YB, Wang PF, Sheng X, et al. Self-engineered lipid peroxidation nano-amplifier for ferroptosis-driven antitumor therapy. *Chem Eng J* 2023;**451**:138991.
12. Yadav P, Ambudkar SV, Rajendra Prasad N. Emerging nanotechnology-based therapeutics to combat multidrug-resistant cancer. *J Nanobiotechnology* 2022;**20**:423.
13. Ye JJ, Yu W, Xie BR, Li K, Liu MD, Dong X, et al. Self-reinforced cancer targeting (SRCT) depending on reciprocally enhancing feedback between targeting and therapy. *ACS Nano* 2022;**16**:5851−66.
14. Yang JJ, Wang XJ, Wang BS, Park K, Wooley K, Zhang SY. Challenging the fundamental conjectures in nanoparticle drug delivery for chemotherapy treatment of solid cancers. *Adv Drug Deliv Rev* 2022; **190**:114525.
15. Bhatia SN, Chen X, Dobrovolskaia MA, Lammers T. Cancer nanomedicine. *Nat Rev Cancer* 2022;**22**:550−6.
16. Yu N, Zhang X, Zhong H, Mu J, Li X, Liu T, et al. Stromal homeostasis-restoring nanomedicine enhances pancreatic cancer chemotherapy. *Nano Lett* 2022;**22**:8744−54.
17. Luo C, Sun J, Liu D, Sun BJ, Miao L, Musetti S, et al. Self-assembled redox dual-responsive prodrug-nanosystem formed by single thioether-bridged paclitaxel-fatty acid conjugate for cancer chemotherapy. *Nano Lett* 2016;**16**:5401−8.
18. Winter JO. One step closer to cancer nanomedicine. *Science* 2022;**377**: 371−2.
19. Lee J, Kim K, Kwon IC, Lee KY. Intracellular glucose-depriving polymer micelles for antiglycolytic cancer treatment. *Adv Mater* 2023;**35**:e2207342.
20. Panagi M, Mpekris F, Chen P, Voutouri C, Nakagawa Y, Martin JD, et al. Polymeric micelles effectively reprogram the tumor microenvironment to potentiate nano-immunotherapy in mouse breast cancer models. *Nat Commun* 2022;**13**:7165.
21. Song YD, Bugada L, Li RT, Hu HX, Zhang LC, Li CY, et al. Albumin nanoparticle containing a PI3Kγ inhibitor and paclitaxel in combination with α-PD1 induces tumor remission of breast cancer in mice. *Sci Transl Med* 2022;**14**:eabl3649.
22. Liu X, Jiang SY, Wang HJ, Wu XH, Yan WJ, Chen Y, et al. Pegylated liposomal doxorubicin combined with ifosfamide for treating advanced or metastatic soft-tissue sarcoma: a prospective, single-arm phase II study. *Clin Cancer Res* 2022;**28**:5280−9.
23. Otsubo K, Kishimoto J, Ando M, Kenmotsu H, Minegishi Y, Horinouchi H, et al. Nintedanib plus chemotherapy for nonsmall cell lung cancer with idiopathic pulmonary fibrosis: a randomised phase 3 trial. *Eur Respir J* 2022;**60**:2200380.
24. Sun LL, Zhao P, Chen MH, Leng JY, Luan YX, Du BX, et al. Taxanes prodrug-based nanomedicines for cancer therapy. *J Control Release* 2022;**348**:672−91.
25. Fang ZX, Lin LQ, Li Z, Gu L, Pan DY, Li YK, et al. Stimuli-responsive heparin-drug conjugates co-assembled into stable nanomedicines for cancer therapy. *Acta Biomater* 2023;**164**:422−34.
26. Mo DC, Ren T. Nivolumab *versus* gemcitabine or pegylated liposomal doxorubicin in patients with platinum-resistant ovarian cancer. *J Clin Oncol* 2022;**40**:522−3.
27. Song ZC, Tian FG, Feng S, Shi LZ, Chen XQ, Liu XH, et al. Pegylated liposomal doxorubicin-induced hand-foot syndrome predicted by serum metabolomic profiling and prevented by calcium dobesilate. *J Am Acad Dermatol* 2022;**86**:688−90.
28. de Lázaro I, Mooney DJ. A nanoparticle's pathway into tumours. *Nat Mater* 2020;**19**:486−7.
29. Wilhelm S, Tavares AJ, Dai Q, Ohta S, Audet J, Dvorak HF, et al. Analysis of nanoparticle delivery to tumours. *Nat Rev Mater* 2016;**1**: 1−12.
30. Mantovani A, Allavena P, Marchesi F, Garlanda C. Macrophages as tools and targets in cancer therapy. *Nat Rev Drug Discov* 2022;**21**: 799−820.
31. Zhang PS, Qiao YY, Zhu LC, Qin M, Li QL, Liu C, et al. Nanoprobe based on biominerals in protein corona for dual-modality MR imaging and therapy of tumors. *ACS Nano* 2023;**17**:184−96.
32. Wang YQ, Zhang LP, Liu Y, Tang LL, He J, Sun XQ, et al. Engineering CpG-ASO-Pt-loaded macrophages (CAP@M) for synergistic chemo-/gene-/immuno-therapy. *Adv Healthc Mater* 2022;**11**: e2201178.

33. Li JH, Huang LJ, Zhou HL, Shan YM, Chen FM, Lehto VP, et al. Engineered nanomedicines block the PD-1/PD-L1 axis for potentiated cancer immunotherapy. *Acta Pharmacol Sin* 2022;**43**:2749−58.
34. Su W, Tan MX, Wang ZH, Zhang J, Huang WP, Song HH, et al. Targeted degradation of PD-L1 and activation of the STING pathway by carbon-dot-based PROTACs for cancer immunotherapy. *Angew Chem Int Ed Engl* 2023;**62**:e202218128.
35. Michel M, Benítez-Buelga C, Calvo PA, Hanna BMF, Mortusewicz O, Masuyer G, et al. Small-molecule activation of OGG1 increases oxidative DNA damage repair by gaining a new function. *Science* 2022;**376**:1471−6.
36. Luo C, Sun BJ, Wang C, Zhang XB, Chen Y, Chen Q, et al. Self-facilitated ROS-responsive nanoassembly of heterotypic dimer for synergistic chemo-photodynamic therapy. *J Control Release* 2019; **302**:79−89.
37. Wang GW, Jiang YF, Xu JJ, Shen JX, Lin T, Chen JF, et al. Unraveling the plasma protein corona by ultrasonic cavitation augments active-transporting of liposome in solid tumor. *Adv Mater* 2023;**35**:e2207271.
38. Yang W, Wang L, Fang ML, Sheth V, Zhang YS, Holden AM, et al. Nanoparticle surface engineering with heparosan polysaccharide reduces serum protein adsorption and enhances cellular uptake. *Nano Lett* 2022;**22**:2103−11.
39. Huang JX, Zhuang C, Chen J, Chen XM, Li XJ, Zhang T, et al. Targeted drug/gene/photodynamic therapy *via* a stimuli-responsive dendritic-polymer-based nanococktail for treatment of EGFR-TKI-resistant non-small-cell lung cancer. *Adv Mater* 2022;**34**:e2201516.
40. Jaaks P, Coker EA, Vis DJ, Edwards O, Carpenter EF, Leto SM, et al. Effective drug combinations in breast, colon and pancreatic cancer cells. *Nature* 2022;**603**:166−73.
41. Zhong YT, Cen Y, Xu L, Li SY, Cheng H. Recent progress in carrier-free nanomedicine for tumor phototherapy. *Adv Healthc Mater* 2023; **12**:e2202307.
42. Zhang HY, Zhao ZQ, Sun SN, Zhang S, Wang YQ, Zhang XB, et al. Molecularly self-fueled nano-penetrator for nonpharmaceutical treatment of thrombosis and ischemic stroke. *Nat Commun* 2023;**14**:255.
43. Sahay G, Alakhova DY, Kabanov AV. Endocytosis of nanomedicines. *J Control Release* 2010;**145**:182−95.
44. Czabotar PE, Garcia-Saez AJ. Mechanisms of BCL-2 family proteins in mitochondrial apoptosis. *Nat Rev Mol Cell Biol* 2023;**24**:732−48.
45. Montero J, Letai A. Why do BCL-2 inhibitors work and where should we use them in the clinic?. *Cell Death Differ* 2018;**25**:56−64.
46. Soderquist RS, Crawford L, Liu E, Lu M, Agarwal A, Anderson GR, et al. Systematic mapping of *BCL-2* gene dependencies in cancer reveals molecular determinants of BH3 mimetic sensitivity. *Nat Commun* 2018;**9**:3513.
47. Ly JD, Grubb DR, Lawen A. The mitochondrial membrane potential (deltapsi(m)) in apoptosis; an update. *Apoptosis* 2003;**8**:115−28.
48. Gottlieb E, Armour SM, Harris MH, Thompson CB. Mitochondrial membrane potential regulates matrix configuration and cytochrome *c* release during apoptosis. *Cell Death Differ* 2003;**10**:709−17.
49. Halestrap AP. What is the mitochondrial permeability transition pore?. *J Mol Cell Cardiol* 2009;**46**:821−31.
50. Sweeney CJ, Martin AJ, Stockler MR, Begbie S, Cheung L, Chi KN, et al. Testosterone suppression plus enzalutamide *versus* testosterone suppression plus standard antiandrogen therapy for metastatic hormone-sensitive prostate cancer (ENZAMET): an international, open-label, randomised, phase 3 trial. *Lancet Oncol* 2023;**24**:323−34.
51. Jiang JH, Slivova V, Jedinak A, Sliva D. Gossypol inhibits growth, invasiveness, and angiogenesis in human prostate cancer cells by modulating NF-κB/AP-1 dependent- and independent-signaling. *Clin Exp Metastasis* 2012;**29**:165−78.
52. Kalla NR, Rovan E, Weinbaue GF, Frick J. Effect of gossypol on prostatic androgen receptors in male rats. *Gossypol: Potent Contracept Men* 1985:111−7.